Journal of Achievements in Materials and Manufacturing Engineering
VOLUME 48
ISSUE 2
October
2011

Effect of the front electrode metallisation process on electrical parameters of a silicon solar cell

L.A. Dobrzański, M. Musztyfaga*
Institute of Engineering Materials and Biomaterials, Silesian University of Technology, ul. Konarskiego 18a, 44-100 Gliwice, Poland
* Corresponding author: E-mail address: malgorzata.musztyfaga@polsl.pl

Received 22.08.2011; published in revised form 01.10.2011

Properties

ABSTRACT

Purpose: This paper shows that the laser micro-treatment of the silicon elements of solar cells with the different morphology of monocrystalline silicon, including the selective laser sintering of the front electrode to its surface using the CO_2 laser, improves the quality by minimising the resistance of a joint between the electrode and the substrate. The influence of the properties achieved for the front electrode on the electrical properties of solar cells was assessed. A front electrode of photovoltaic cells deposited by the traditional screen printing method and by co-firing in the infrared conveyor furnace was prepared for comparative purposes.
Design/methodology/approach: The topography of front contacts subjected to selective laser sintering and co-firing in the infrared conveyor furnace was investigated using the scanning electron microscope with the energy dispersive X-ray (EDS) spectrometer for a microchemical analysis and with the confocal laser scanning microscope. Both, the surface topography and cross section of the front contacts was examined with the SEM microscope. The phase composition analyses of the selected front contacts were carried out using the XRD method. The front contacts were formed on the surface with the different morphologies of solar cells: textured ones with a coated antireflection layer, textured ones without a coated antireflection layer, non-textured ones with a coated antireflection layer and non-textured ones without a coated antireflection layer. An average size of pyramids was measured using the atomic force microscope (AFM). The resistance of the front electrodes was investigated using the Transmission Line Model (TLM).
Findings: The following technological recommendations for the laser micro-treatment technology such as optimal paste composition, the power and scanning speed of the laser beam, the morphology of the silicon substrate to produce the front electrode of silicon solar cells, were selected experimentally in order to produce a uniformly melted structure, well adhering to the substrate, with the low resistance of the front electrode-to-substrate joint zone.
Research limitations/implications: The contact resistance of front metallisation established depends on the paste composition, morphology of the silicon substrate as well as the co-firing and laser micro-treatment conditions.
Originality/value: This paper investigates the front contact production using different silver paste compositions on silicon solar cells in order to decrease contact resistance and increase efficiency in this way.
Keywords: Electrical properties; Front electrode; Silicon solar cell; Selective laser sintering; Screen printing

Reference to this paper should be given in the following way:
L.A. Dobrzański, M. Musztyfaga, Effect of the front electrode metallisation process on electrical parameters of a silicon solar cell, Journal of Achievements in Materials and Manufacturing Engineering 48/2 (2011) 115-144.

1. Introduction

One of the manufacturing process operations for photovoltaic cells is to produce a front electrode having an appropriate shape and size, and also a hollow in the semiconductor material. This issue has been widely discussed in a great deal of research papers. Connections are formed in the connection zone of electrodes on the front and back sides of the semiconductor ensuring extra resistance limiting the flow of photocurrent into an electric circuit [1-14].

These losses are minimised by applying pastes from which contacts are made and the level of emitter doping is determined [15]. Current leaks are occurring in the connection area, separated from a charge carrier connected with a crystal lattice defect (e.g., microcracks). Photo voltage drop is seen in a solar cell as a consequence. Examples are provided further on of improvement in solar cell efficiency during its manufacturing process: good electrode adhesion to the silicon surface and low resistivity of the connection zone between the electrode and silicon [16-25].

The field of the front contact surface is a compromise between electrical and optical losses caused by shading [26]. It is very important to design appropriately, both, the size and shape of the front electrode in order to minimise these losses. Among others, resistance between the front electrode connection zone and the silicon surface has an effect on the losses of a photovoltaic solar cell and this is also the main subject of studies into its electrical properties. The resistance of the metal-semiconductor connection zone depends on the composition of the conductive paste or metal powder from which the paths were made, as well as on the manufacturing conditions [17, 27-39].

The following resistance: series (R_s) and parallel (R_{sh}) resistance both influence a power loss in a solar cell and the shape of the I-V curve [16].

Series resistance (R_s) is a sum of individual layers in a photo element (Fig. 1). R_3 to R_6 resistance relates both, to the shape and quality of the front electrode silicon solar cell [19, 40]. Parallel

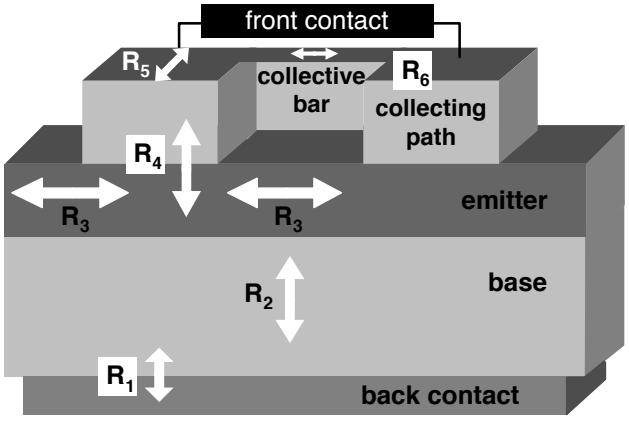

Fig. 1. Scheme of series resistance: R_1 – metal-semiconductor, R_2 – semiconductor material (base), R_3 – emitter between collecting paths of front electrode, R_4 – metal-semiconductor, R_5 – the collecting path of front electrode, R_6 – collective bar of front electrode [19, 16, 25, 40, 41]

resistance (R_{sh}) stems from a current leakage along the solar cell periphery and along the dislocation and grain borders. Current leakages are caused by micro-cracks and other structural defects. Power losses in solar cells characterised by improved quality caused by parallel resistance are insignificant as compared to the losses caused by series resistance. The fill factor (FF) depends largely on the both factors (R_s and R_{sh}) [19, 16, 25, 40, 41].

Various deposition and fabrication techniques are applied to improve the electrical properties of electrodes (Fig. 2) [15, 16, 42-76]. The main subject of the studies described in this article is a manufacturing process based on the application of the modern selective laser sintering and classical screen printing methods connected with their co-firing in the furnace.

Selective Laser Sintering (SLS) is a modern manufacturing technique using the high-power CO_2 laser to melt or sinter, in precisely definite areas, metal powder particles into the mass with the expected three-dimensional shape. The micro-treatment process is controlled with this method via a computer program [35, 36, 57-61, 77]. The following stages of the front contacts formation process can be distinguished between for this method [78]:

1. a silicon wafer is placed onto a table in a chamber for sintering, next the table is lowered by a preset value,
2. metallic powder is spread uniformly on the silicon wafer with a special drift fender,
3. the excess metallic powder is removed into a container as it can be re-used,
4. the powder is heated locally with a laser beam and metal lines on the top of the wafer are melted as required, following the determined paths, and the layers of the spatial object are next applied in a similar manner,
5. the cycle is repeated.

Screen printing (SP) is performed on, both, the front and the back sides of silicon solar cells. A screen is located in this method within the specific distance underneath the upper part of the silicon wafer. Metallic (e.g. silver) paste is placed on the screen, printed using two squeegees. One of the squeegees is used to deposit the paste evenly, the other is used to force the paste trough the screen onto the silicon wafer surface. Each screen printing process can be divided into the three major phases [19, 25, 57, 58, 60]:

1. overprinting collection back contacts (Al/Ag) and dry,
2. overprinting a front electrode (Ag) and drying,
3. co-firing the front and back metal contacts.

Studies into the literature present a screen printing method for coating and co-firing a front electrode in the furnace. Nevertheless, material factors and manufacturing conditions are influencing the quality when applying powders and pastes and it is necessary to being experiments anew.

There are some examples in the literature, however, of front metallisation manufacturing through selective laser sintering [79]. These examples have inclined the authors to adopt an approach as presented herein. The paper concentrates primarily on the studies the purpose of which is to ensure the front electrode manufacturing conditions by applying silver powders with varied grain size (being the paste component) with the laser technique becoming an essential part of the contemporary photovoltaic technology.

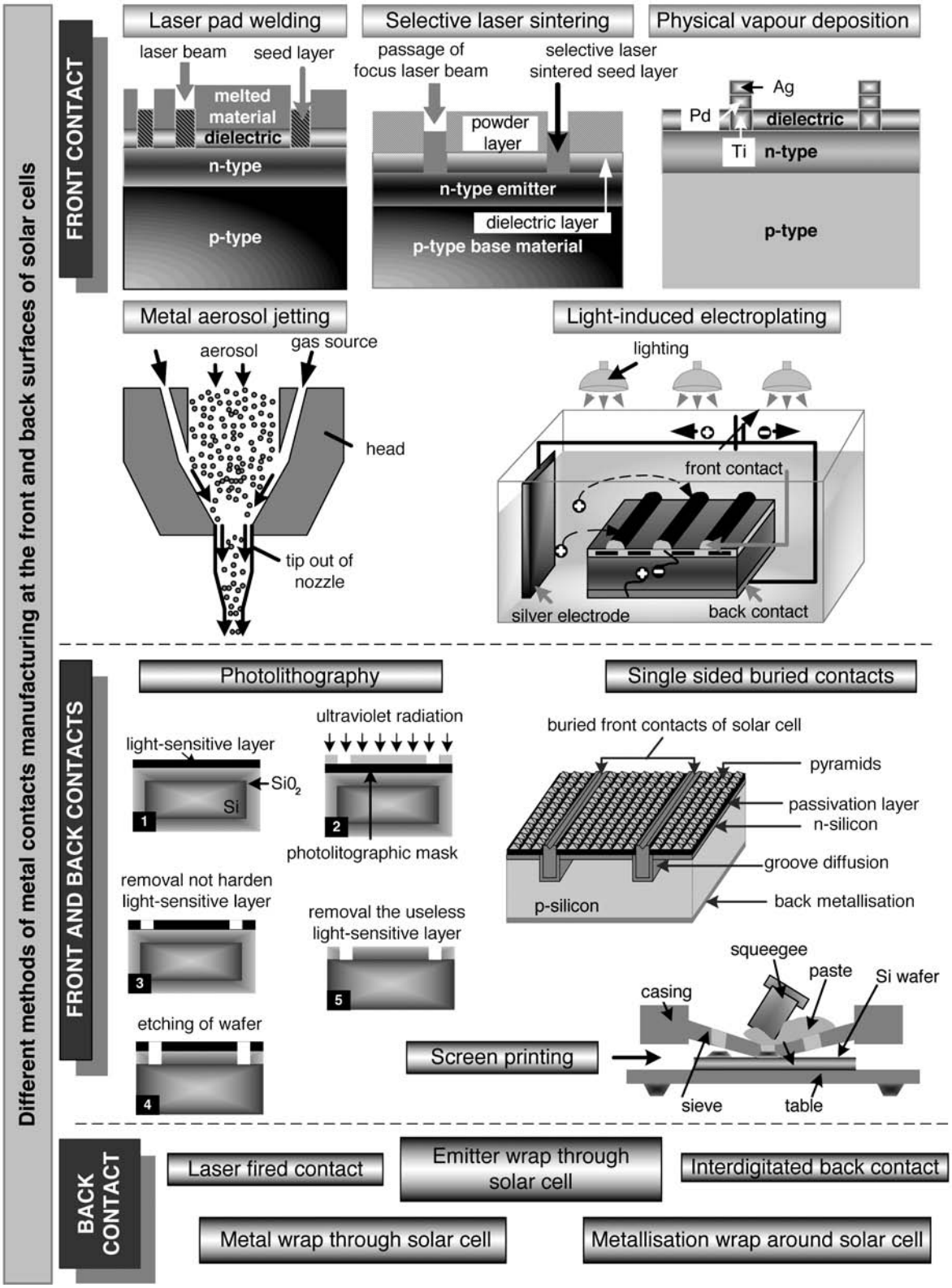

Fig. 2. Methods of manufacturing electrical contacts of solar cells

2. Experimental procedure

The investigations were carried out on monocrystalline silicon wafers manufactured by Deutsche Solar AG (Germany). The shape and size of the wafers is shown in Fig. 3. The material properties of the silicon used in this paper are presented in Table 2.1. ~330 µm thick wafers were processed with the SLS method, whereas those approx. ~230 µm thick were processed with the SP method and co-fired in the furnace.

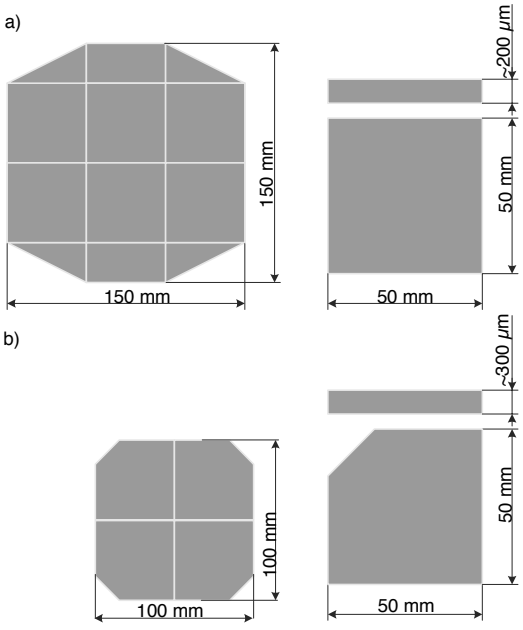

Fig. 3. Shapes and sizes of monocrystalline wafers after cutting with a diamond saw: a) 200 ± 30 µm thick, b) 330 ± 10 µm thick

Table 2.1.
The basic parameters of the two grades of the silicon used

Type	p	p
Doped	boron	boron
Thickness	200 ± 30 µm	330 ± 10 µm
Area	5 cm x 5 cm	5 cm x 5 cm
Resistivity	1-3 Ω·cm	~1 Ω·cm
Carbon concentration	$8x10^{16}$ at/cm^3	$\leq 1x10^{18}$ at/cm^3
Oxygen concentration	$1x10^{18}$ at/cm^3	$\leq 2x10^{17}$ at/cm^3

Two silver powders with the grain size of 40 µm (Fig. 4 a, Table 2.2) and 40 nm (Fig. 4 b, Table 2.3) were applied during the investigations according to the metallographic observations of the front electrode manufactured using the SLS method in order to determine the optimal grain size and powder. The paste properties of the overprinted contact layer of the solar cell are presented in Table 2.4. The chemical composition of the front contact was selected experimentally and mixtures were prepared using a mechanical stirrer.

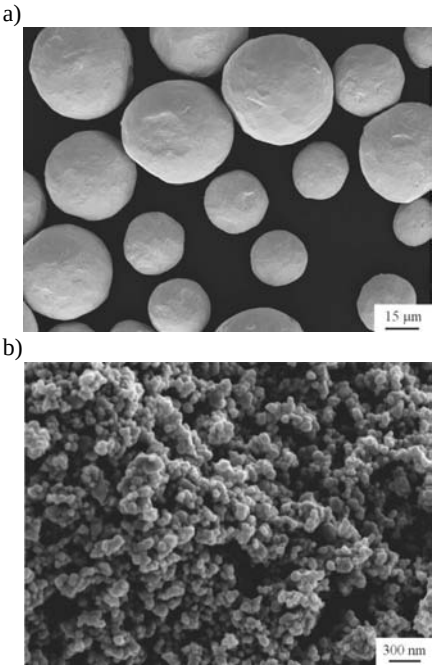

Fig. 4. SEM micrographs of silver powder: a) grain size of <40 µm, b) grain size of <40 nm

Table 2.2.
Mass concentration of silver powder elements

Mass concentration of elements, % *			Flow rate of powders sec/50 g **	Density, g/cm^3 **	
Ag	Na	Others		Bulk	Tab
99.9	0.05	indefinite	14	5.8	21.76

***** - according to the supplier's certificate, ****** - based on Hall cone

Table 2.3.
Mass concentration of silver nanopowder elements

Mass concentration of elements, % *		
Ag	Al, Bi, Cd, Cr, Fe, Mg, Mo, Ni, Sb, Zn, As, Ca, Co, Cu, K, Mn, Na, Pb, Ti, Zr	Others
99.95	<0.0205	indefinite

***** - according to the supplier's certificate

The technology of solar cells has been developed at the Institute of Metallurgy and Materials Science of the Polish Academy of Science in Cracow (Poland). The solar cells manufacturing process for solar cells with the different morphology of silicon (100) consists of the following steps:

- chemical etching,
- formation of p-n junction,
- formation of parasitic junction,
- surface passivation of solar cells (SiO_2),
- antireflection coating (TiO_x) deposition ,
- screen printing of front contacts,
- co-firing in the furnace front contacts,
- selective laser sintering of front contacts.

Table 2.4.
Paste properties

Paste symbol	Mass concentration of elements, %			Surface morphology of the solar cells
	Basic powder	Organic carrier	Ceramic glaze	
Selective laser sintering				
A	83	15	2	1, 2, 3, 4
B	88.40	9.60	2	1, 2, 3, 4
Co–firing in the furnace				
C	88.40	11.60	-	1, 2
D	85	15	-	3, 4
E	60.60	39.40	-	1, 2
F	83.33	16.67	-	3, 4
PV145*	-	-	-	1, 2, 3, 4

Comment: 1 – Non-textured solar-cells with the deposited TiO_x coating, 2 – Non-textured solar-cells without the deposited TiO_x coating, 3 – Textured solar-cells with the deposited TiO_x coating, 4 – Textured solar-cells without the deposited TiO_x coating, * commercial paste manufactured by Du Pont

One of the important aspects of this paper was to produce test electrodes systems (Fig. 5). The front electrodes were produced in order to demonstrate that silver pastes are useful and to evaluate the contact resistance of the silver electrode-silicon junction.

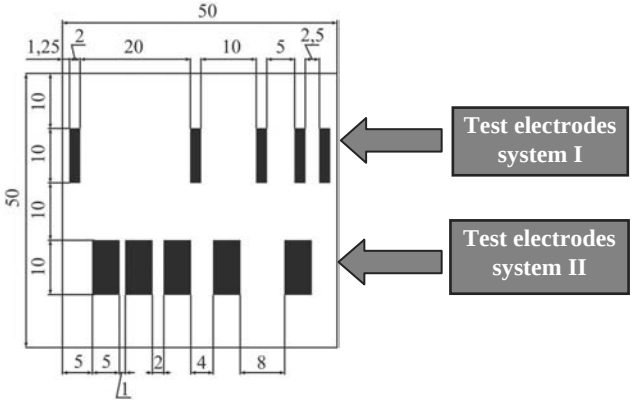

Fig. 5. Test front electrode system overview

Three initial series for testing the solar cells were first prepared though laser micro-treatment (Table 2.5) in order to achieve the smallest resistance value of the connection zone between the electrode and the silicon substrate of the solar cell and a uniform structure. The most advantageous conditions of laser micro-treatment were selected based on the tests and metallographic observations. The selected laser micro-treatment conditions for the tested electrodes system I, II are provided in Table 2.6. Table 2.7 presents the general data of the device used.

Table 2.5.
Initial conditions of laser micro-treatment for testing the electrodes of silicon wafers cleaned chemically

Series	Paste symbol	Laser beam feed rate (v), mm/s	Laser beam (P), W	Front electrode thickness, µm
1	PV 145	50-200	8.1-37.8	15, 40, 60
2	A	50-200	21.5-48.6	15, 35, 70
3	B	50-200	10.8-48.6	40, 60, 80

Table 2.6.
Conditions of the laser micro-treatment of the test electrodes of silicon solar cells made from the A paste

Series	Solar cell surface	Front electrode thickness, µm	Laser beam feed rate (v), mm/s			Laser beam (P), W
1	1-4	15, 35	37.8	40.5	43.2	50
2	1-4	15, 35	48.5	51.3	54	100
3	1-4	60	21.6	24.3	27	50

Comment: 1 – Non-textured solar-cells with the deposited TiO_x coating, 2 – Non-textured solar-cells without the deposited TiO_x coating, 3 – Textured solar-cells with the deposited TiO_x coating, 4 – Textured solar-cells without the deposited TiO_x coating

Table 2.7.
Technical specification of the Eosint M 250 Xtended device [77]

Laser beam feed rate	max. 3.0 m/s
Laser beam output power	270 W
Laser beam diameter	300 µm
Wavelength	10640 nm
Shielding gas	nitrogen

Figure 6 shows a system for the laser treatment of silicon solar cells. In case of co-firing, some solar cells were made with the I, II test electrodes system in the conveyor-type IR furnace (Table 2.8). The conveyor IR furnace was equipped with tungsten filament lamps, heating both the top and the bottom of the conveyor (the conveyor belt feed rate was 200 cm/min).

Table 2.8.
Conditions of co-firing in the furnace testing electrodes of silicon solar cells (the front electrode thickness of: 15, 40, 60 µm)

Series	Paste symbol	Temperature, °C		
		Zone I	Zone II	Zone III
1	C, D	530	570	830
				860
				890
				920
				945
2	PV 145	530	570	830
				860
				890
				920

a)

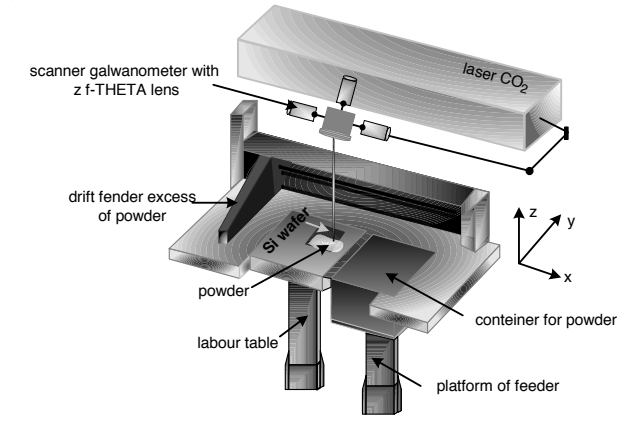

b) c)

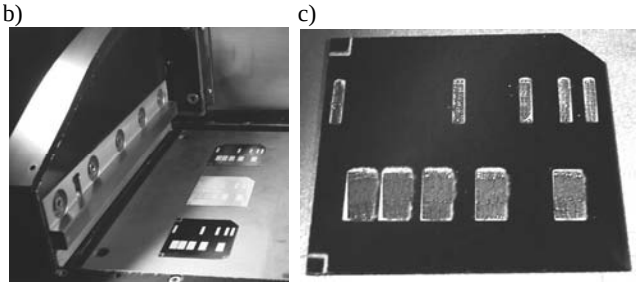

Fig. 6. Laser-treatment system: a) EOSINT M 250 Xtended device equipped with CO_2 laser, b) working chamber in which silicon solar cells are located with test electrode systems, c) solar cell after SLS

An R_T resistance measurement for the tested electrode with the transmission line method was calculated for a short series (N=3), i.e. by making 3 measurements for each pair of the adjacent paths of front electrodes on the monocrystalline silicone surface of the investigated sample. The following three current values were used during the investigations: 10, 30 and 50 mA.

An arithmetic mean was calculated for the set of measurement results according to the following formula (2.1):

$$\overline{R_T} = \frac{1}{N} \cdot \sum_{n=1}^{N} R_T \tag{2.1}$$

A limited set of results selected from the entire set of measurements using the linear regression method enabled to determine the L_T and R_c coefficients sought for. Random errors were found using the estimation of the u_C standard complex uncertainty often performed in practice, presented by the A-type uncertainty. They are the sum of the normal distribution and apparatus errors presented by the B-type uncertainty assumed using uniform distribution. These errors are, in principle, mutually independent [41]. The u_C standard complex uncertainty of the resistance measurement (R_T) was estimated taking into account the apparatus errors (B-type uncertainty) according to the following algorithm:

I. The u_A A-type standard uncertainty was determined:

For the limited set of measurements (N<10, N=3), where N means a number of measurement results in the set. The $\overline{R_T}$ arithmetic mean was determined using the following formula:

$$\overline{R_T} = \frac{1}{N} \cdot \sum_{n=1}^{N} R_{Tn} \tag{2.2}$$

The $s_{\overline{R_T}}$ standard deviation of an arithmetic mean was determined using the following formula:

$$s_{\overline{R_T}} = \frac{s_{R_T}}{\sqrt{N}} \tag{2.3}$$

where:

$$s_{R_T} = \sqrt{\frac{1}{N-1} \cdot \sum_{n=1}^{N} (R_{Tn} - \overline{R_T})^2} \tag{2.4}$$

For the standard A- type uncertainty:

- it is assumed that the α confidence level fulfilling a quintile in normal distribution equals the standard deviation of a single measurement result;
- the k number degrees of freedom is calculated according to the formula:

$$k = N - 1 \tag{2.5}$$

- the $t_{k,\alpha}$ quintile is determined using the Table of distribution for the k calculated and the α established. A confidence level was determined for the factors confidence of 1-α=0.95, and k=2 and finally determined as $t_{k,\alpha}$=4.3027 [80];
- the A-type standard uncertainty was calculated using the following formula:

$$u_A(R_T) = t_{k,\alpha} \cdot S_{\overline{R_T}} \tag{2.6}$$

where: R_{T1}, R_{T2}, ..., R_{TN} – a set of measurements

II. The u_B B-type standard uncertainty is determined using the documents and certificates available for the measuring apparatuses. It is assumed that the B-type uncertainty is characteristic for uniform distribution and its certainty level is within the ±a range in respect of the correct value.

Then the B-type standard uncertainty is determined using the formula:

$$u_B(R_T) = \frac{a}{\sqrt{3}} \tag{2.7}$$

Considering that resistance is determined using two apparatuses, the correct value equals the boundary instrumental resistance measurement R_X :

$$a = \Delta R_X \tag{2.8}$$

The formula of the R_X boundary instrumental resistance measurement with resistance being determined according to the formula, follows from the formula:

$$\Delta R_X = \sqrt{\left(\frac{\delta R}{\delta U}\Delta U\right)^2 + \left(\frac{\delta R}{\delta I}\delta I\right)^2} = \sqrt{\left(\frac{\Delta U}{I}\right)^2 + \left(\frac{\Delta I \cdot U}{I^2}\right)^2} \tag{2.9}$$

hence:

$$u_B(R_T) = \frac{\Delta R_X}{\sqrt{3}} = \frac{\sqrt{\left(\frac{\Delta U}{I}\right)^2 + \left(\frac{\Delta I \cdot U}{I^2}\right)^2}}{\sqrt{3}} \tag{2.10}$$

However, the result obtained will have its accuracy depending on the measuring apparatuses applied, especially their accuracy, i.e. the boundary errors of both $\pm\Delta U$ – voltmeter and $\pm\Delta I$ – direct current calibrator.

III. The u_C standard complex uncertainty for the formula is determined using the formula:

$$u_C(R_T) = \sqrt{u_A^2(R_T) + u_B^2(R_T)} \tag{2.11}$$

The u_C standard complex uncertainty can be extended, so one can calculate the half-width of the range where the error is presented with increased probability for the probability ratio set up for the standard uncertainty. U_c is extended for this purpose until the α certainty level is reached and u_C is multiplied by the adequate k_α. factor. The accurate determination of k_α is difficult, so to simplify this, two cases are considered in the literature:

(a) $u_A \geq u_B$ – then A-type uncertainty dominates normal distribution or A-type uncertainty, close to B-type uncertainty,

(b) $u_A < u_B$ – then B-type uncertainty dominates steady distribution.

The k_α values are determined from the table recommended from literature in order to choose the values of the certainty level. The k_α factor value equals 1.960 – in the (a) case; 1.645 – in the (b) case, for the determined α=0.05 certainty level (probability of 95 %).

IV. Finally, the complex uncertainty was determined using the following formula:

$$R_T = \bar{R}_T \pm k_\alpha u_C(R_T) \tag{2.12}$$

with the following comment added: ”where the number provided after ± symbol is a value of the standard u_C complex uncertainty, but it is not a certainty interval”.

The following investigations were performed in this paper:

- the estimation of grain fraction for silver powders using two analyzers. For silver nanopowder, a new laser particle sizer analysette by Fritsch, based on the diffraction of He – Ne laser rays, was applied. The investigation was performed according to PN-ISO 9276-1 standard. In case of ceramic glaze and silver micrometric powder, the Kamika Instruments IPSUA analyzer was used. Three independent measurements were taken using SiO_2 particles size. The main measurement was made with the resolution of 4096 of dimensional classes, in order to make 256 equal dimensional classes or 12 any given screens available to the user. An identical procedure was applied in case of silver powder. In order to analyze the possible inorganic elements in the preparation of ceramic glaze, its sample was burnt using the X-ray diffraction fluorescence (XRF);
- the chemical analyses of ceramic glaze were performed: the proton (1H) and carbonic (13C) spectra on the spectroscope techniques most widely used nowadays: Nuclear Magnetic Resonance (NMR) allowing to recognise the carbon and hydrogen atom signals in a different chemical environment using the pulse spectrometer – UNITY/INOVA 300 MHz (Varian) type, the infrared spectrum (IR), was registered with an FTIR Nicolet 6700 spectrometer determining the presence of functional groups in the analyzed preparation;
- the topography of a silicon wafer with texture using the atomic force microscope (Park Systems XE 100) in the non-contact mode. The medium size of the pyramids was also measured using this microscope;
- the R_c contact resistance, ρ_c specific contact resistance and (L_T) transfer length of a front contact solar cell using the Transmission Line Model (TLM) method onto a measuring position were determined at the Institute of Engineering Materials and Biomaterials. TLM consists in a direct current (I) measurement and a voltage (U) measurement between any two separate contacts;
- measurement results were collected and next the necessary calculations and analyses of the obtained data were performed;
- the electrical properties of the solar cells were examined with front metallisation performed conventionally and performed in a non-conventional manner on a computerised Solar – Lab positioning table. The procedure consisted of measuring I-V curves of the photovoltaic solar cells to determine the 1.5 radiation spectrum with the radiation intensity of 1000 W/m^2 and also the solar cell temperature of 25°C. The I-V characteristics were established by fitting the measured I-V plots with the theoretical two-diode model using the Solar Fit program. The following values were determined with this program: dark currents (I_{s1} and I_{s2}) and photocurrent (I_p), series resistance (R_s) and parallel resistance (R_{sh}), A_1 and A_2 diode quality factors;
- a phase composition analysis of the chosen front contacts using the XRD method;
- a microchemical analysis of the chosen front contacts using the scanning electron microscope equipped with the energy dispersive X-ray (EDS) spectrometer;

- the topography of, both, the surface and cross section of front contacts using:
  - a Zeiss Supra 35 scanning electron microscope (SEM) using secondary electron detection with the accelerating voltage between 5-20 kV;
  - a Zeiss confocal laser scanning microscope (CLSM**)** with its source of light being the diode laser with the capacity of 25 mW emitting radiation with the wavelength of 405 nm. The contact thickness profile was determined with six average measurements;
  - the thickness of the tested front electrodes was measured using the SEM and CLSM.

3. Results and discussion

Figure 7 presents the results of a grain size analysis of the silver nanopowder from Laser Particle Sizer Analysette 22. It was found by measuring the grain size of the nanopowder that a considerable portion has its diameter close to this declared by the manufacturer.

It was found based on the results obtained presented in Table 3.1 that 75.42% of SiO_2 particles, by volume, reveal the average grain size of >10 μm. However, for silver powder (Ag), the volume of the particles within the range of < 40 μm is 78.84%. A ceramic glaze sample was burnt (the weight of the sample to be burnt was 13.3121 g) and the weight of the ash produced after the investigation is very small (0.008 g) (Table 3.2).

The results of a chemical analysis of ceramic glaze are presented in Figs. 8-10. It was found based on the investigations that the proton spectrum (1H) reveals a complex aliphatic system (Fig. 8) and the presence of small signals was found there for the range characteristic for unsaturated systems. Neither ether nor ester groups were found, however. For carbonic spectrum (13C), the presence of signals was found in the unsaturated and aliphatic systems (Fig. 9). Low signal was also determined likely to confirm the presence of the amine group. Infrared spectrum (IR) confirms the presence of the amine group and other carbonyls (Fig. 10) and the strands of an unsaturated system. The adherence of the amine strand was also found.

Table 3.1.
Fraction distribution 1 – total volumetric portion of grains

No	Sieves, μm	SiO_2	Ag (<40 μm)
		Volumetric portion of particular grain class (Bv), %	
1	70	0.23	0.01
2	60	0.57	0.14
3	50	1.02	2.02
4	45	1.58	4.08
5	40	2.58	21.16
6	35	4.55	61.65
7	30	8.17	85.63
8	25	14.83	93.42
9	20	26.43	97.58
10	15	45.97	99.45
11	10	75.42	99.95
12	bottom	100	100

Table 3.2.
Results of sample burning at the temperature of 400°C – analysis by the XRF method on the ZSX Primus spectrometer using SQX program for a half – quantitative analysis

Chemical element	Concentration in deposit after incineration, %	Concentration in sample after counting,%
Na	39.3197	0.0236
Mg	2.5733	0.0015
Si	3.0544	0.0018
P	3.6752	0.0022
S	10.148	0.0061
Cl	4.435	0.0027
K	3.2187	0.0019
Ca	27.9418	0.0168
Fe	4.3178	0.0026
Ni	0.6071	0.00036
Zn	0.1553	0.00009
Ag	0.339	0.00020
Pb	0.2146	0.00013

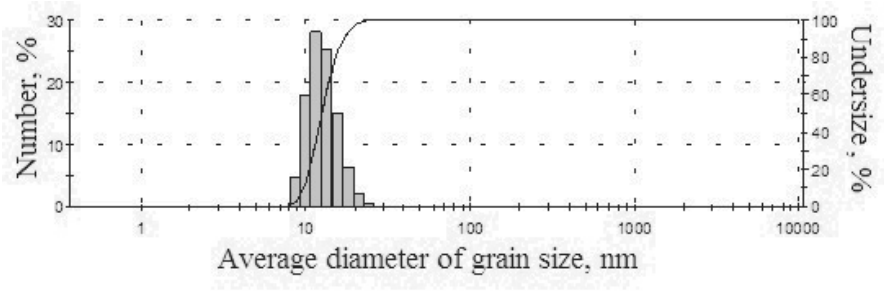

Fig. 7. Histogram of distribution according to number and distribution undersize silver nanopowder

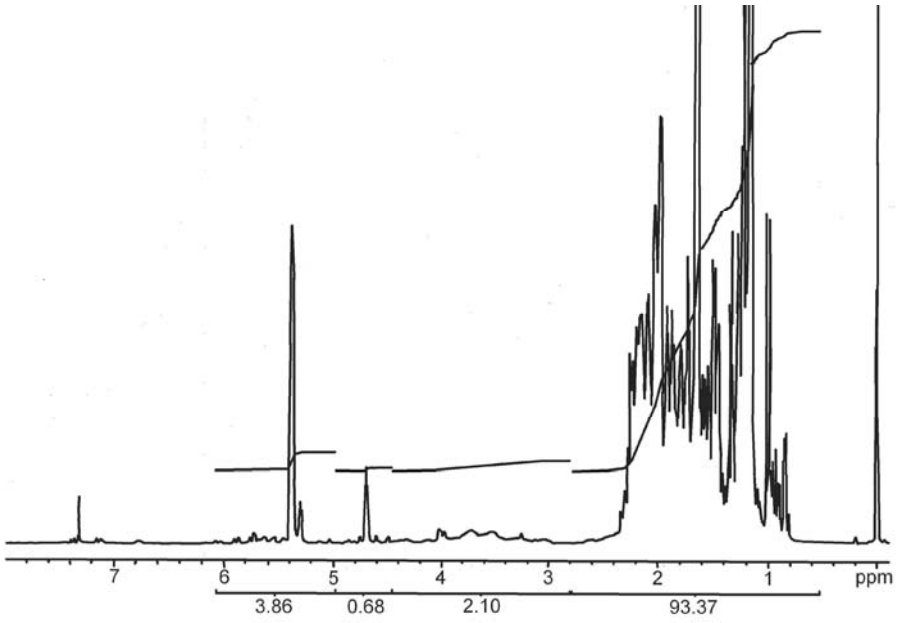

Fig. 8. Proton spectrum (1H) nuclear magnetic resonance (NMR) of ceramic glaze

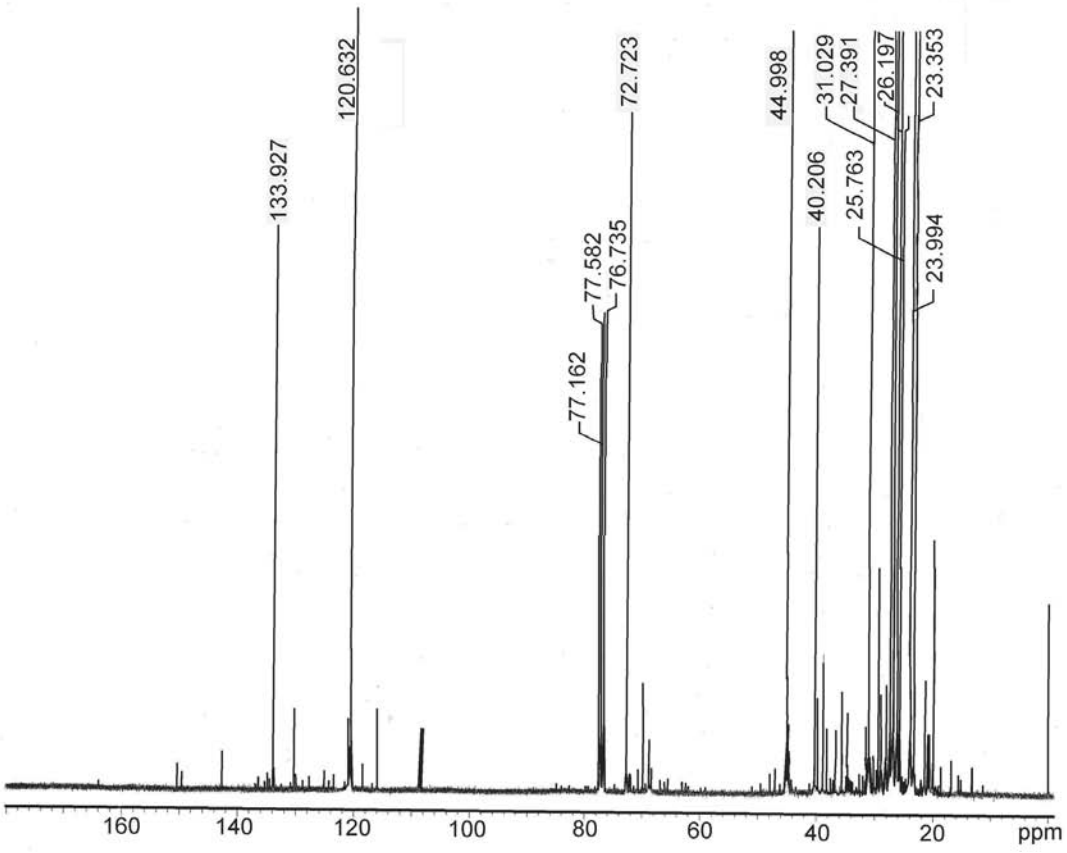

Fig. 9. Carbonic spectrum (13C) nuclear magnetic resonance (NMR) of ceramic glaze

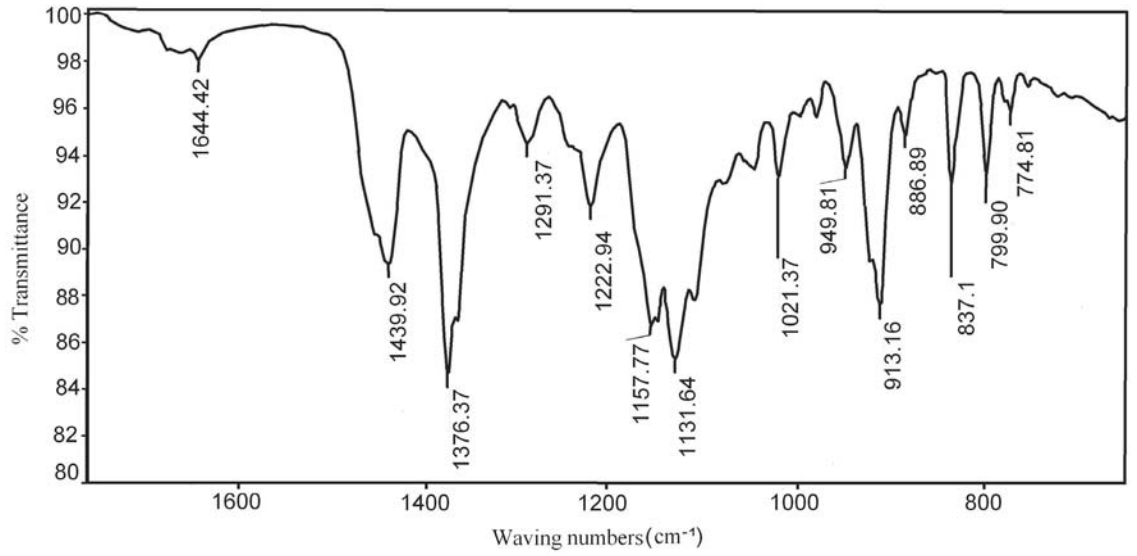

Fig. 10. Infrared spectrum (IR) of ceramic glaze (sample)

a) b) c)

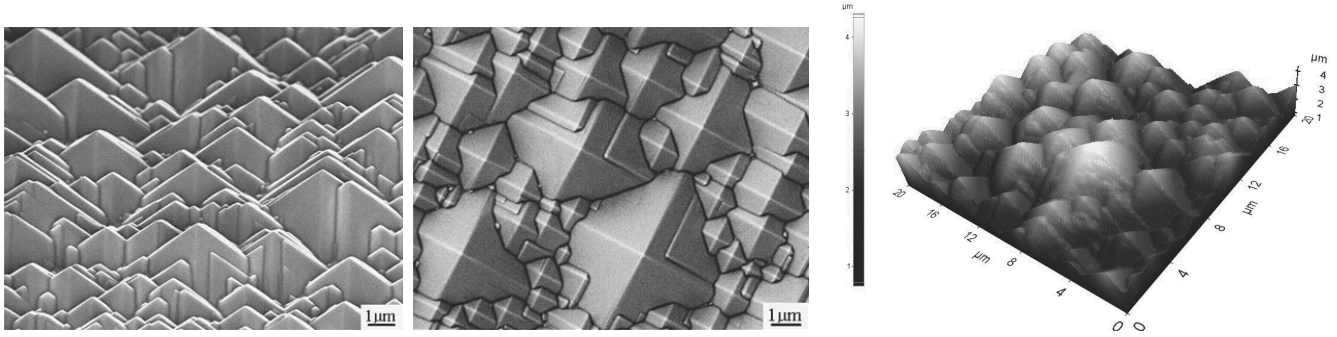

Fig. 11. Topography of the textured surface of a monocrystalline solar wafer with the thickness of: a) 200 µm, b) 300 µm (SEM), c) 300 µm (AFM)

The topographies of the silicon wafers were observed with texture in the atomic force microscope. The average thickness of pyramids of 3 µm was determined with the atomic force microscope (Fig. 11).

Based on metallographic observations (Fig. 12) it was found that in SLS technology is not possible to apply silver pastes to deposit front electrodes (about regular shape and uniform thickness) using EOSINT M 250 Xtended device.

Figures 13 b, c, d show the front electrode structure with the test system – selective laser sintering from the standard PV 145 paste. It was found based on the metallographic observations of structures, that the grain size of electrodes vary, similarly as for an electrode structure made of the same paste before its micro-treatment (Fig. 13 a). Metallographic investigations confirm that this electrode did not sinter (Fig. 13 b, c). It was also found in metallographic observations (Fig. 13) that, with the SLS technology, it is not possible to apply silver pastes to deposit front electrodes (with regular shape and uniform thickness) using the EOSINT M 250 Xtended apparatus.

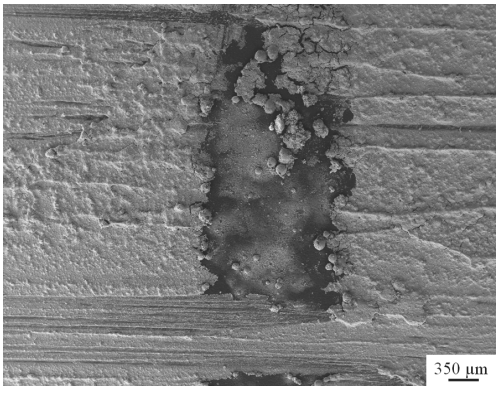

Fig. 12. Surface topography of the layer deposited from A paste onto the silicon substrate and laser sintered with the laser beam with the feed rate of 100 mm/s and the laser beam capacity of 32.4 W

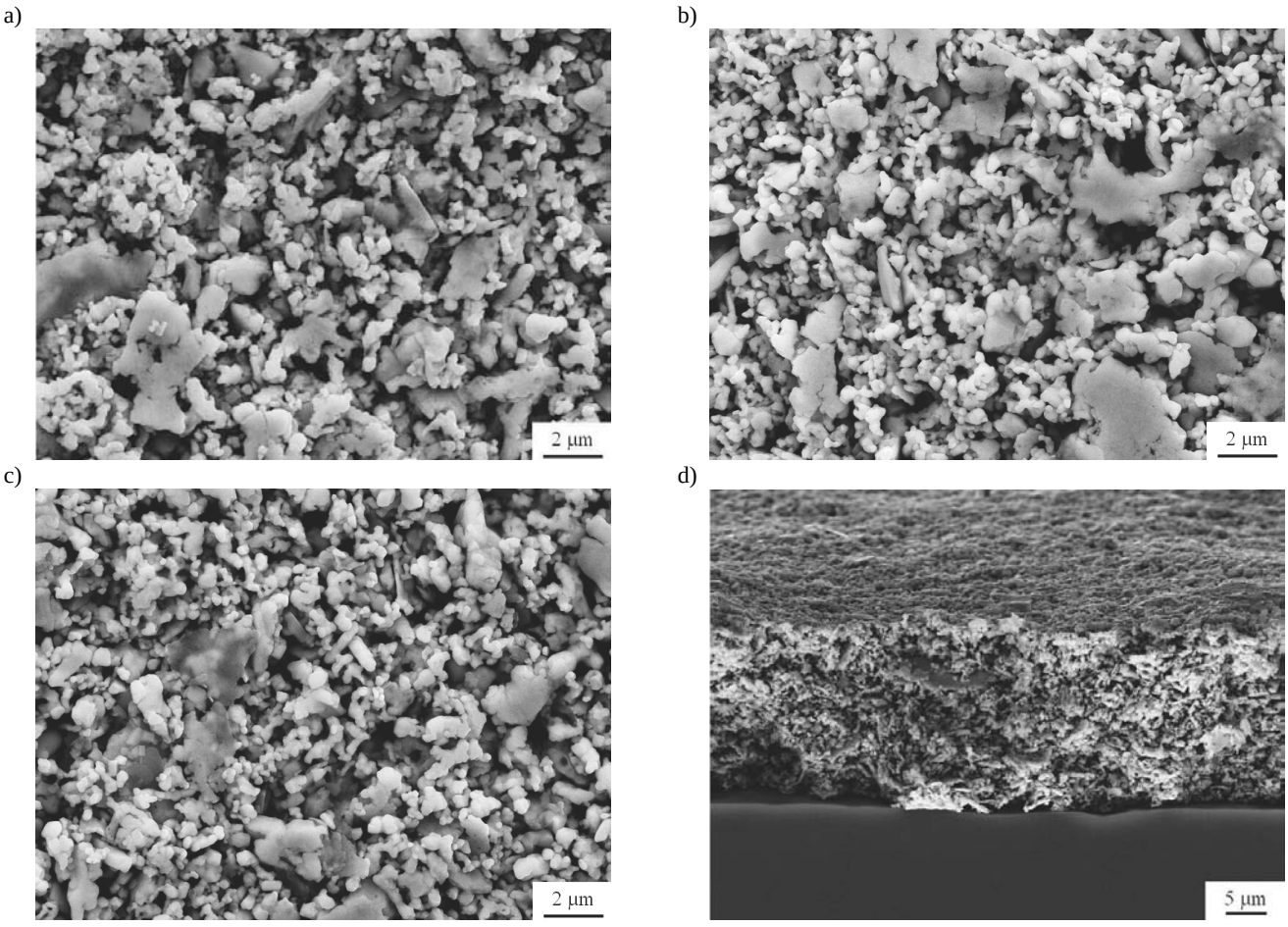

Fig. 13. Surface layer topography (with the average thickness of 15 µm) made from PV 145 paste on the silicon surface and deposited with the screen printing method: a) did not sinter, b) selective laser sintered with the laser beam feed rate of 50 mm/s and laser beam power of 27 W, c) selective laser sintered with the laser beam feed rate of 50 mm/s and laser beam of 32.4 W, d) fracture of front electrode from figure c (SEM)

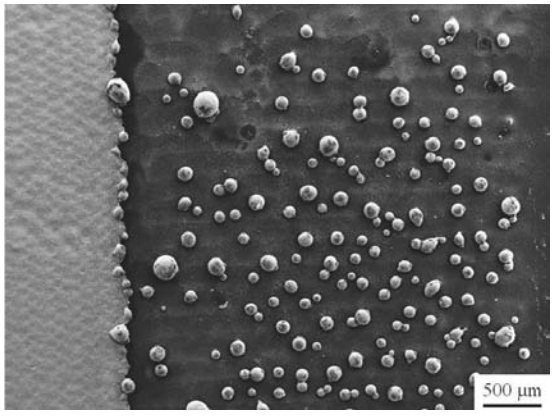

Fig. 14. Surface layer topography (with the average thickness of 15 µm) made from PV 145 paste on silicon surface and selective laser sintered with the laser beam feed rate of 50 mm/s and laser beam power of 35.1 W (SEM)

If a laser beam's capacity is increased, the electrode is completely burnt and evaporates (Fig. 14). As a result of the investigations carried out, the authors have withdrawn from applying the PV 145 standard in their further work. Figures 15 b, c present the front electrode structure from the test system – selective laser sintered from the A paste. It was found through the metallographic observations of structures, that the electrodes made of grains have varied size and spherical shape, similarly as in the electrode structure prepared from the same paste before its micro-treatment (Fig. 15 a). Metallographic investigations confirm that with the so selected laser micro-treatment conditions, the front electrode does not sinter. Figure 15 d shows the partial evaporation of the electrode, the melting of elements, as well the areas of the fully exposed silicon substrate in the electrode. The authors decided as a result of the investigations to resign in their further work from the selective laser sintering of the I, II test electrode system silicon solar cells with the average thickness of 70 µm from the A paste. The test structures of the front electrodes formed with selective laser sintering from the B paste

are shown in Figs. 16 a and 17 a. It was found when observing these structures that the grains form numerous spherical agglomerates of silver balls with varied sizes (from a few to a dozen or so micrometers). This occurs individually on the electrode surface or forms the connected clusters of two or more agglomerates. Metallographic examinations confirm that with the selected conditions of laser micro-treatment processes taking place in the electrode layer, the contact points of the contacting particles are included only. A more homogenous structure was produced for the maximum feed rate of the laser beam of P=27 W. This occurred by melting silver powder grains and through melting them together (Figs. 16 b and 17 b). The areas of complete exposure of the silicon substrate in electrodes were revealed. Based on the results obtained, the authors decided to give up further investigations for the selective laser sintering of the electrode system I, II silicon solar cell with the average thickness of 40 and 80 μm from B paste.

As a result of macroscopic and microscopic investigations, the conditions of laser micro-treatment were selected for the test electrode system I, II and for the collecting electrode of the photovoltaic solar cell by selecting additionally for this purpose, the smallest value of specific resistance (ρ_c) of the test electrodes.

Based on the investigations of electrical properties using the TLM method, it was found in the first series (Table 2.6) that the smallest specific contact resistance values of the I, II test electrodes system are, respectively, 0.17-0.57 $\Omega \cdot cm^2$ and 0.53-1.63 $\Omega \cdot cm^2$ for solar cells with different morphology. The minimum specific contact resistance value was obtained for the I, II I, II test electrodes system (0.17 $\Omega \cdot cm^2$; 0.53 $\Omega \cdot cm^2$) with the average thickness of 35 μm on the substrate without texture and without a TiO_x coating applied with a laser beam of 37.8 W and the laser beam feed rate of 50 mm/s. It was found based on the investigations of electrical properties using the TLM

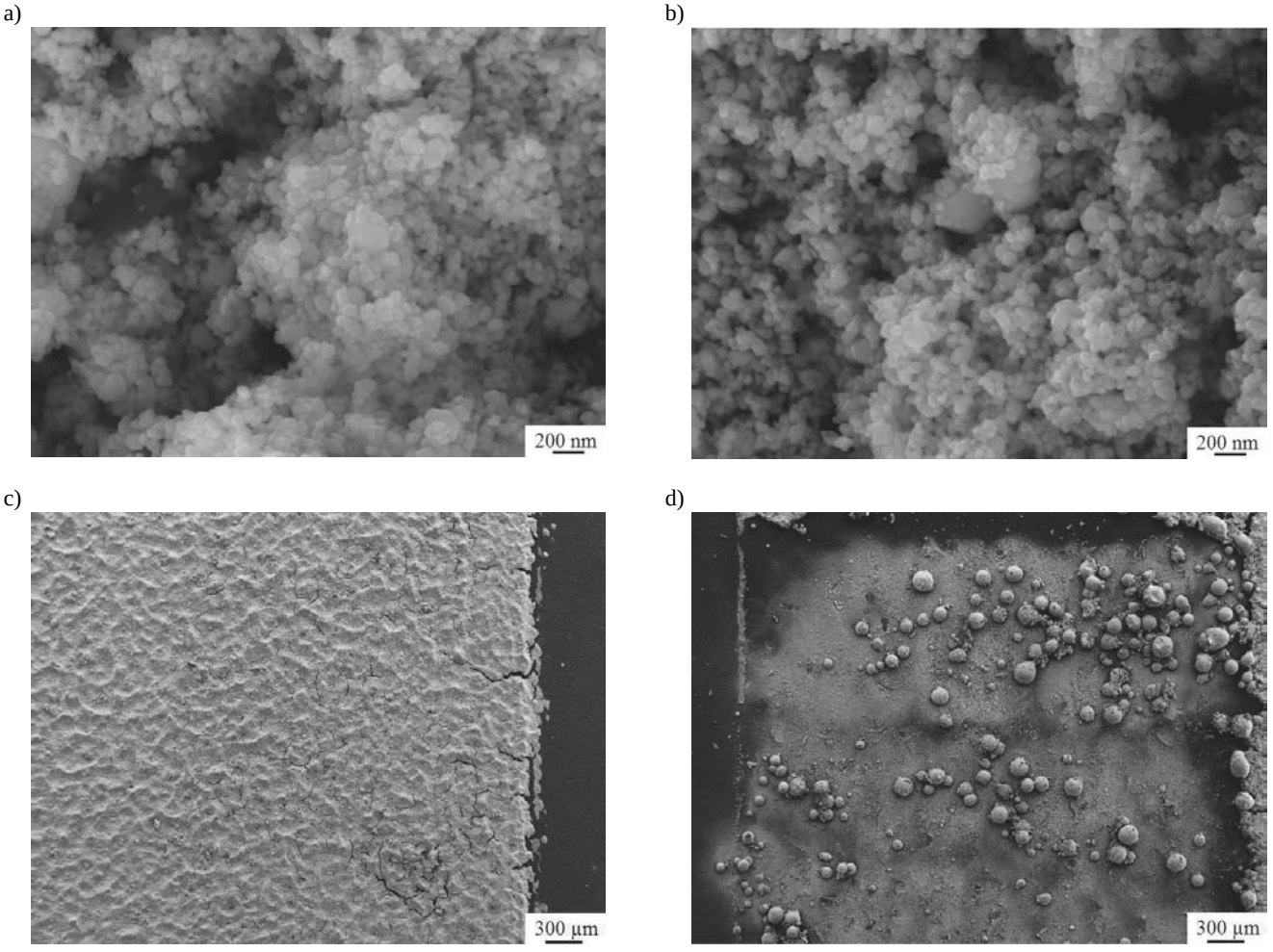

Fig. 15. Surface layer topography (with average thickness of 70 μm) obtained from A paste on silicon surface and deposited by screen printing method: a) did not sinter, b) selective laser sintered with the laser beam feed rate of 50 mm/s and minimum laser beam power of 31.5 W, c) the surface layer topography from figure b, d) laser sintered with the laser beam feed rate of 50 mm/s and maximum laser beam power of 40.5 W (SEM)

a) b)

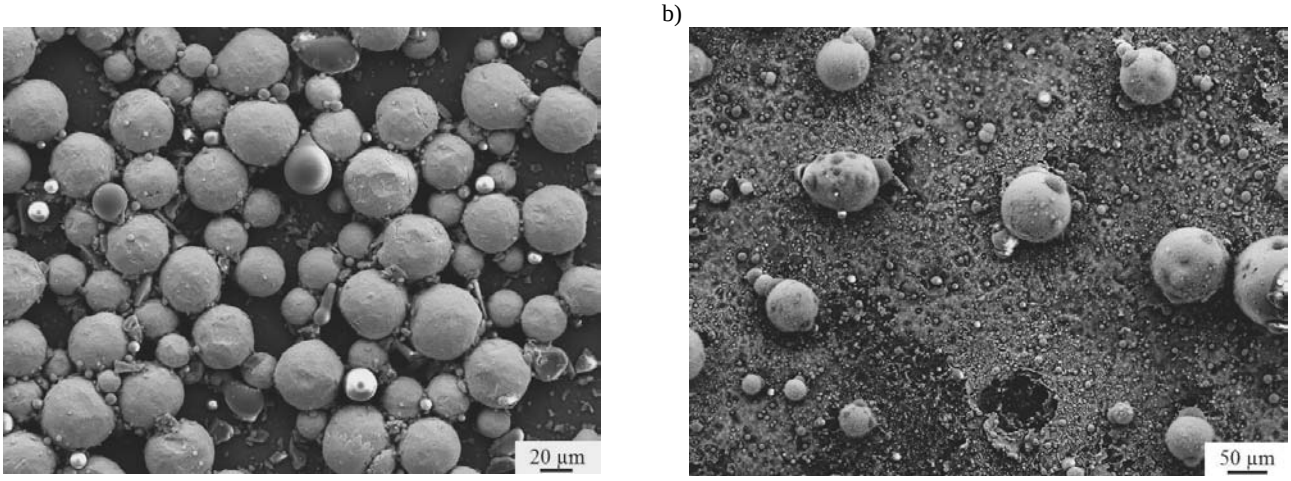

Fig. 16. Surface layer topography (with the average thickness of 40 µm) obtained from the B paste on silicon surface by selective laser sintering with the laser beam feed rate of 50 mm/s and a) minimum laser beam power of 10.8 W, b) maximum laser beam power of 27 W (SEM)

a) b)

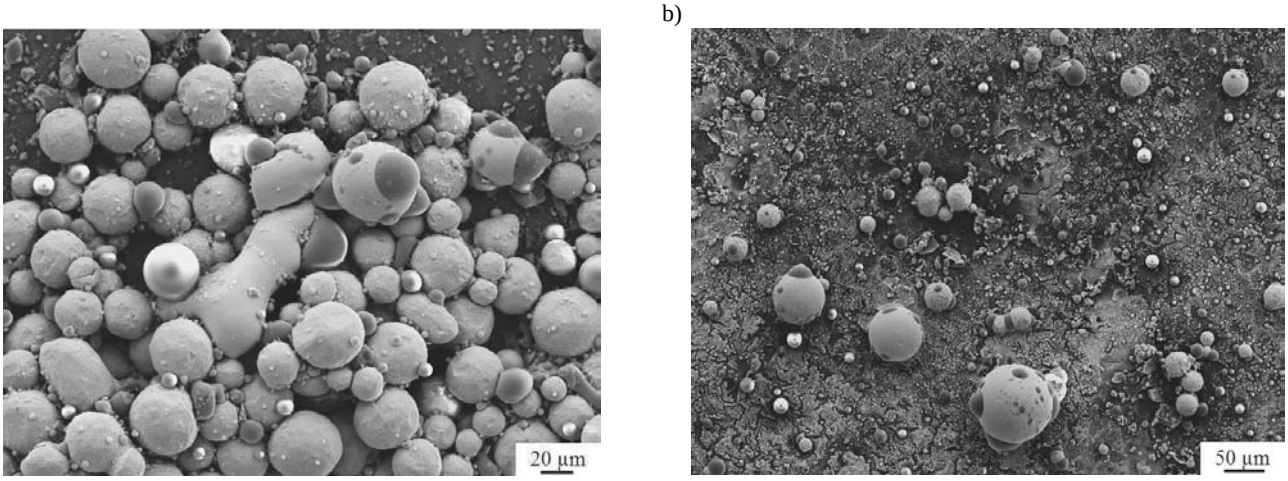

Fig. 17. Surface layer topography (with the average thickness 80 µm) obtained from the B paste on silicon surface with selective laser sintering with the laser beam feed rate of 50 mm/s and a) minimum laser beam power of 10.8 W, b) maximum laser beam power of 27 W (SEM)

method in the second series (Table 2.6) that the smallest specific contact resistance values of the I, II test electrodes system test electrodes system are 0.01-0.77 $\Omega \cdot cm^2$, 0.68-2.82 $\Omega \cdot cm^2$, respectively, for solar cells with different morphology. The minimum specific contact resistance value was obtained for the I test electrodes system (0.01 $\Omega \cdot cm^2$, P=51.3 W), II (0.68 $\Omega \cdot cm^2$, P=48.6 W) with the average thickness of 35 µm on the substrate without texture and without a TiO_x coating applied with the laser beam feed rate of 100 mm/s.

It was found, therefore, that the morphology of a silicon substrate has significant influence on obtaining a minimum resistance value of the electrodes produced through selective laser sintering from the A paste. It is higher for a substrate with texture than for the one without texture. It is probably connected with the occurrence of empty areas under contacts as the average thickness of the pyramids textured surface for Si (100) is between 3 to 9 µm. An antireflective coating prevents the reflection of sunbeams and energy losses. It also provides a barrier for the connection zone improving resistance between the electrode layer and the silicon substrate. The thickness of the deposited layer influences the structure of the electrode layer produced and the resistance value of the resistance electrode. It was found that the SLS test contacts with the average thickness of 35 µm exhibit both, the good adhesion of the layers to the silicon substrate. However, the test

contacts with the average thickness have the areas of total exposure of the silicon substrate and damages to their layer in form of micro-cracks probably caused by thermal stresses due to a cooling rate during laser micro-treatment.

It was found with the investigations of electrical properties using the TLM method in the third series (Table 2.6) that the smallest specific contact resistance values of the I, II I, II test electrodes system are 0.02-0.78 $\Omega \cdot cm^2$, 0.11-1.01 $\Omega \cdot cm^2$, respectively, for solar cells with different morphology. A minimum specific contact resistance value was seen for the I, II I, II test electrodes system (0.02 $\Omega \cdot cm^2$; 0.11 $\Omega \cdot cm^2$) with the average thickness of 60 µm on a substrate without texture and without a TiO_x coating applied with a laser beam of 24.3 W and a laser beam feed rate of 50 mm/s. Some differences were found for the results of measurements for the test electrode systems prepared from the B paste. This fact can be explained by the heterogeneity of the deposited metallic layer in form of a columnar structure with pores and a heterogeneous zone of the connection electrode with the silicon substrate of a solar cell.

It was determined with the investigations of electrical properties using the TLM method that the smallest specific contact resistance is recorded in the second series (Table 2.8) of the I, II test electrodes system formed of PV 145 paste. The minimum specific contact resistance value within the temperature range of 860-920°C of the I, II test electrodes system is 1.08-2.73 $\Omega \cdot cm^2$ and 0.48-1.33 $\Omega \cdot cm^2$ for solar cells with different morphology. The highest range of specific contact resistance was found in the first series (Table 2.8) for front contacts made of C, D pastes. The minimum specific contact resistance value of the I, II test electrodes system within the temperature of 860-945°C

a) b)

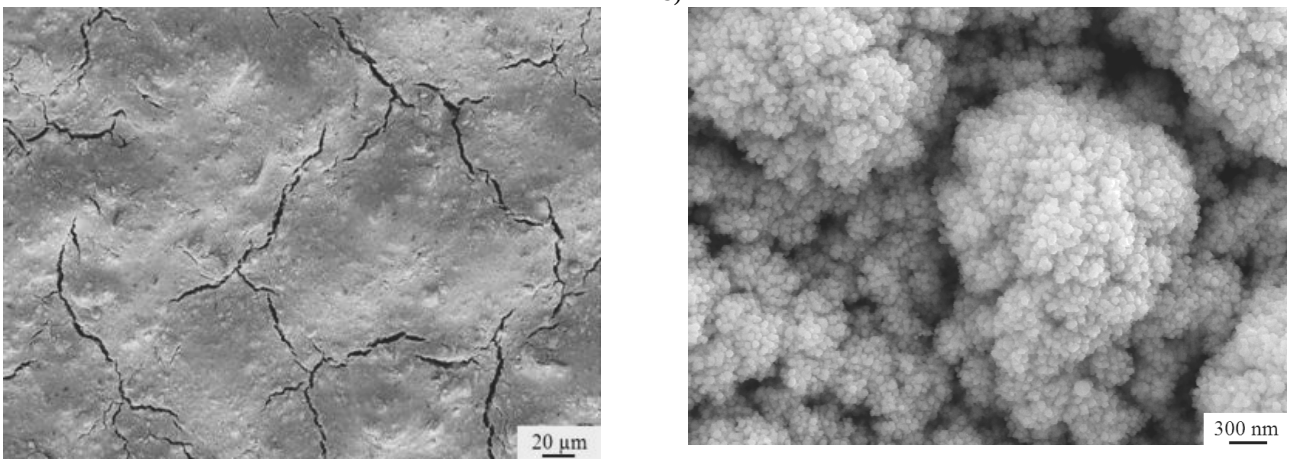

Fig. 18. SEM images of the front contact layer prepared from A paste and selective laser sintering with the laser beam power of 40.5 W and the laser beam feed rate of 50 mm/s on an Si substrate without texture and a) with ARC layer, b) without ARC layer

a) b)

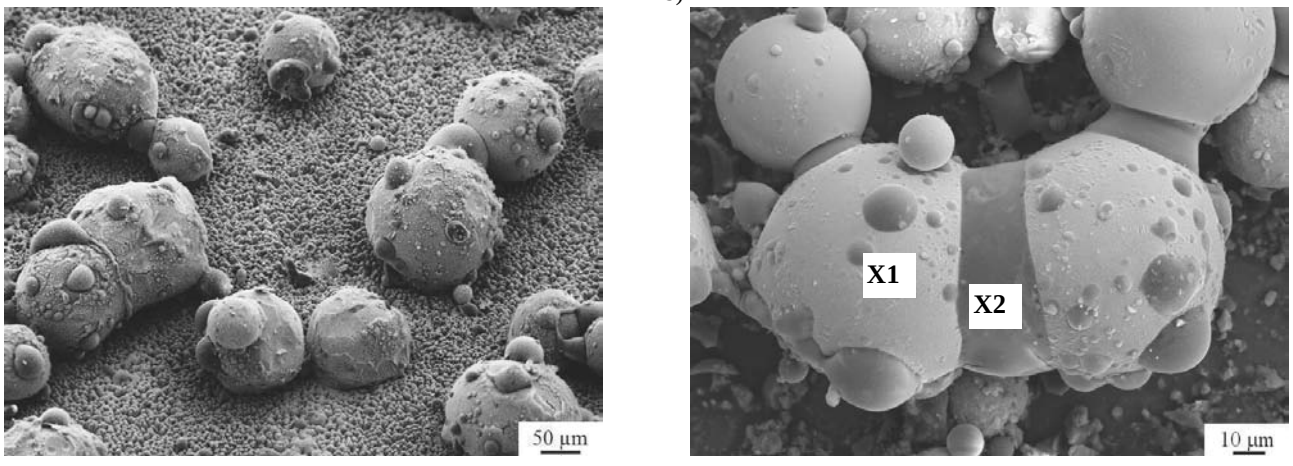

Fig. 19. SEM images of front contact layer from B paste on the surface with texture and ARC layer by selective laser sintering with the feed rate of laser beam travel of 50 mm/s and the laser beam of a) 24.3, b) 13.5 W

is 1.83-86.81 Ω·cm^2 and 1.12-71.63 Ω·cm^2 for solar cells with different morphology. The investigations of electrical properties with the TLM method confirm that paste resistance decreases as the electrode co-firing temperature increases due to the declining resistance of connection between metallic grains. Contact resistance was found to be growing along with a temperature increase. This is probably caused by the molten silver molecules forming huge agglomerates and voids would develop under contacts for a textured surface. The contact layers prepared from the PV 145 paste provide many homogenous connections with the silicon substrate while contact layers made with the C, D pastes create point connections. The stability of electrical measurements with TLM method was ensured for the A paste with the average thickness 35 µm of the test electrodes system, however, this influence was not confirmed for the PV 145 paste.

It was determined through metallographic observations that the front electrodes prepared from silver nanopaste and selective laser sintering have their structure uniformly melted, often with irregular shapes showing a lattice of micro-cracks in some places (Fig. 18 a). A distinct granular structure is shown clearly in highly magnified pictures (Fig. 18 b).

It was also stated that the front electrodes sintered with selective laser based on silver micrometric powder reveal a significant heterogeneity connected with the occurrence of numerous agglomerates in the silver globule shape with varied sizes ranging from several to tens of micrometers (Figs. 19 and 20).

The observations in the scanning electron microscopy allow to conclude that the morphology of the test electrode system deposited with the PV 145 paste and co-fired in the furnace has a porous structure. Moreover, the electrodes prepared show a structure with their varied density grades depending on the co-firing temperature. The front electrodes solar cells formed at the lowest co-firing temperature (830°C) exhibit a more porous structure than the electrodes sintered at the highest temperature (945°C) indicating a very homogenous structure as a consequence of contact pitting and their melting (Fig. 21).

a)

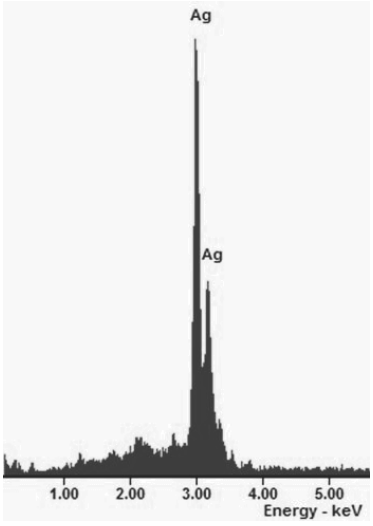

b)

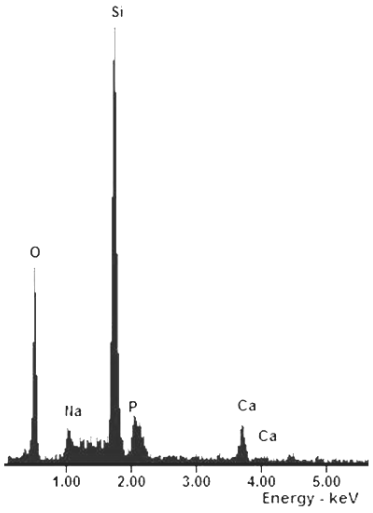

c)

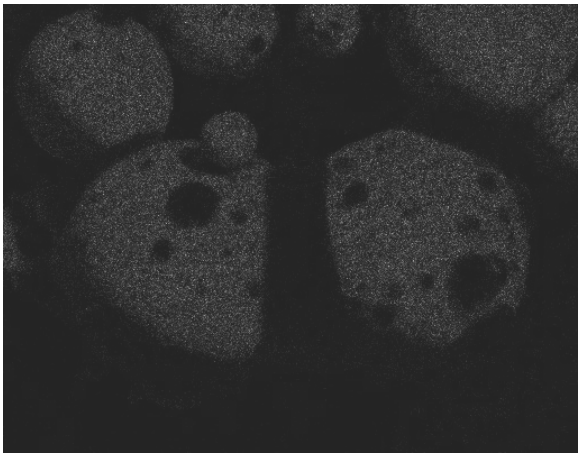

d)

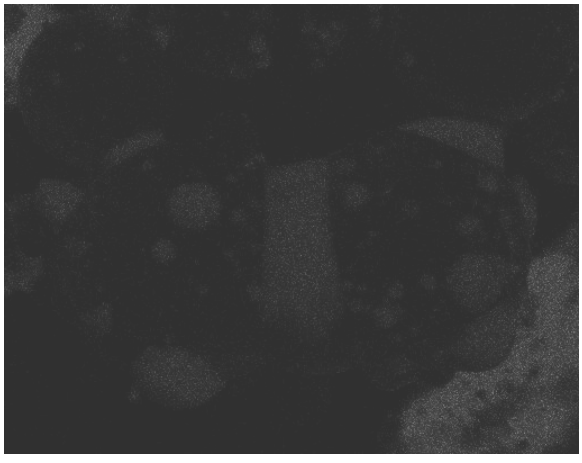

Fig. 20. Plot of energy dispersion X-rays from micro-areas in Fig. 19b: a) X1, B) X2. Maps of superficial distribution of elements from the area in Fig. 19b: c) Ag, d) Si

a) b)

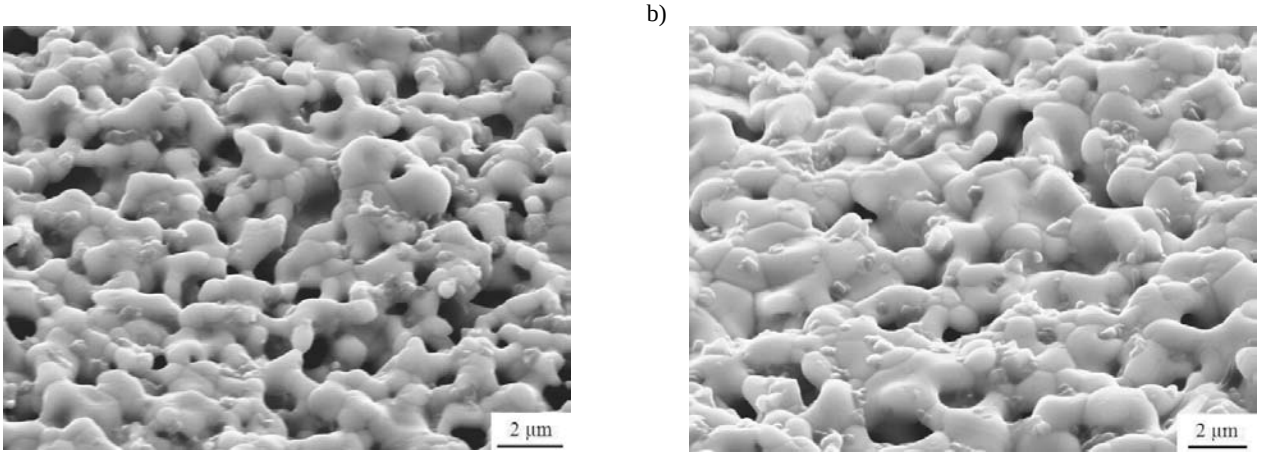

Fig. 21. SEM images of front contact layer prepared from PV 145 paste and co-fired in the conveyor furnace at the temperature of a) 830°C, b) 920°C on the Si substrate without texture and ARC layer

a) b)

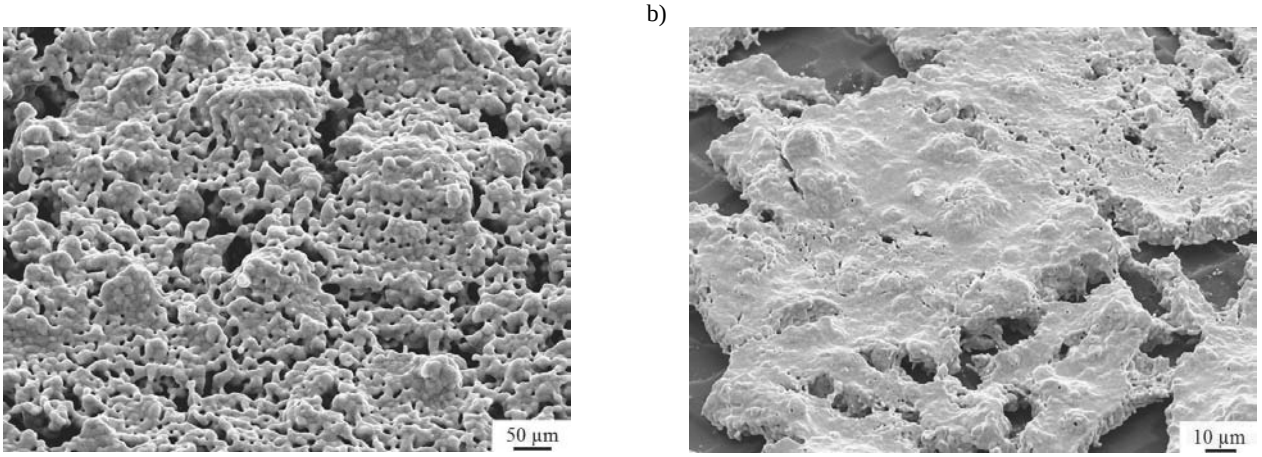

Fig. 22. SEM images of the front contact layer prepared from the C paste and co-fired in the conveyor furnace at the temperature of a) 945°C, b) 830°C on an Si substrate without texture and with an ARC layer

a) b)

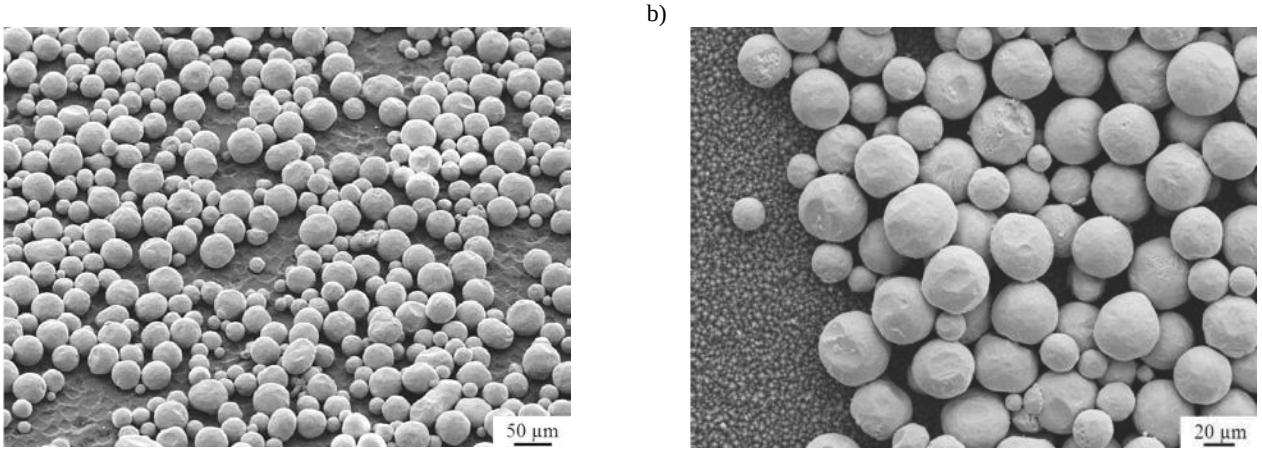

Fig. 23. SEM images of the front contact layer prepared from: a) E paste and co-fired in the furnace at the temperature of 830°C on an Si substrate without texture and with an ARC layer, b) F paste and co-fired in the furnace at the temperature of 830°C on an Si substrate with texture and without an ARC layer

It was determined for the test electrode system produced with silver nanopowder-based pastes and co-fired in the furnace that the compound structure features numerous cracks on the entire electrode surface (Fig. 22). In addition, these electrodes demonstrated a porous structure similar to the one formed in co-firing with the standard PV 145 paste. Their porosity level was increasing along with the co-firing temperature, similar as for the commercial paste.

It was identified for the test electrode system prepared from silver powder-based pastes and co-fired in the furnace that the individual grains of the electrode were interconnected in a point-wise manner leading to the high porosity of the electrodes. Besides, some areas were found where the entire silicon substrate inside the electrode was not covered (Fig. 23).

The thickness of the test electrodes was determined by checking the height profile of the three-dimensional surface topography measured using the confocal laser scanning microscope (Fig. 24).

Tables 3.3 to 3.5 list the results of thickness measurements for front electrodes co-fired in the furnace on silicon substrates. The thickness for the test front electrodes co-fired at the lowest temperature of 830ºC does not increase or decrease and the thickness is low in relation to the thickness of the electrodes before firing (Table 3.3).

Table 3.3.
Thickness comparison of the front electrodes deposited from the PV 145 paste and co-fired in the furnace

Solar cell surface	Co-firing temperature, °C III zone	Average electrode thickness, µm		
		SEM		CLSM
		before co-firing	after co-firing	
1	830	15	15	15
	920		13	12
2	830	15	14	14
	920		11	11
3	830	30	29	29
	920		28	28
4	830	40	27	20
	920		23	20

Comment: 1 – Non-textured solar-cells with the deposited TiO_x coating, 2 – Non-textured solar-cells without the deposited TiO_x coating, 3 – Textured solar-cells with the deposited TiO_x coating, 4 – Textured solar-cells without the deposited TiO_x coating

The thickness of the test electrodes co-fired at the highest temperatures of 920ºC and 945ºC with PV 145 and of the test electrodes sintered with selective laser from the A and B paste decreases slightly versus the thickness of the electrodes before sintering. As a result of SEM investigations, the examined test front electrodes sintered with selective laser reveal the diverse cross-section thickness of between 570 nm to 2.3 µm.

Table 3.4.
Comparison of thickness of the front electrodes deposited from the C, D pastes and co-fired in the furnace

Solar cell surface	Co-firing temperature, °C III zone	Average electrode thickness, µm		
		SEM		CLSM
		before co-firing	after co-firing	
1	830	15	11	14
	945		10	12
2	830	15	14	13
	945		12	12
3	830	35	34	30
	945		32	25
4	830	70	68	68
	945		62	65

Table 3.5.
Comparison of thickness of the front electrodes deposited from the E, F pastes and co-fired in the furnace

Solar cell surface	Co-firing temperature, °C III zone	Average electrode thickness, µm		
		SEM		CLSM
		before co-firing	after co-firing	
1	830	40	38	39
	945		35	36
2	830	40	39	38
	945		37	45
3	830	60	56	57
	945		53	54
4	830	80	79	77
	945		74	74

It was found with the fractographic investigations of the test front electrode system of the silicon solar cells prepared from the A paste and subjected to selective laser sintering that well concentrated layers without pores and discontinuities are obtained for the electrodes produced, well adhering to the silicon substrate (Fig. 25 a). Moreover, the structure of the test electrode photo-voltaic cell prepared from the B paste and subjected to selective laser sintering shows columnar forms with pores (Fig. 25 b).

A finding was made according to fractographic investigations that the test electrodes made of the standard PV 145 paste through co-firing in the conveyor furnace method demonstrated a bondage with the substrate without defects and delaminations. An electrode layer creates many homogenous connections with the silicon substrate close to the continuous connection (Fig. 26 a). For electrodes prepared from silver powder, the connection between the electrode and silicon is pointwise, independently of the sintering temperature applied and silicon morphology (Fig. 26 b). The connections of electrodes made from pastes based on silver nanopowder are pointwise, only the places close to the continuous connection (Fig. 26 c).

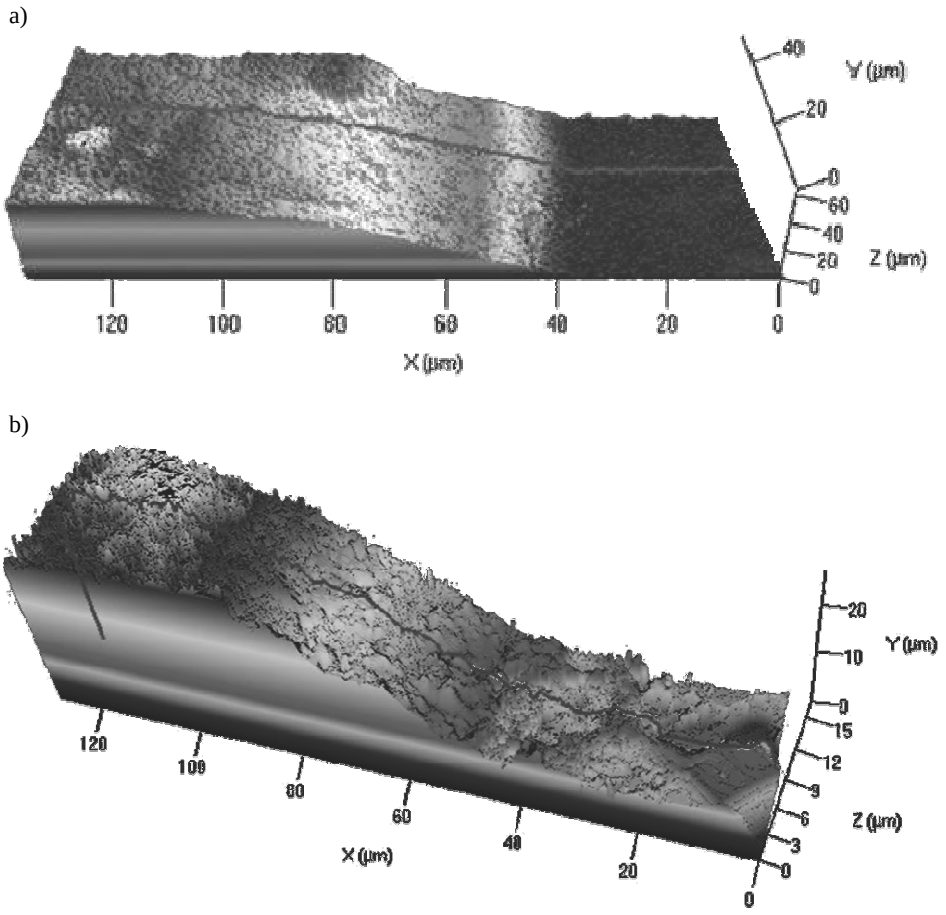

Fig. 24. Three-dimensional surface topography (CLSM) of the front electrode prepared from: a) the A paste on a surface without texture and with ARC layer subjected to selective laser sintering with the laser beam of 40.5 W and the laser beam feed rate of 50 mm/s, b) the PV 145 on a surface without texture and an ARC layer co-fired in the furnace at 920°C temperature (example)

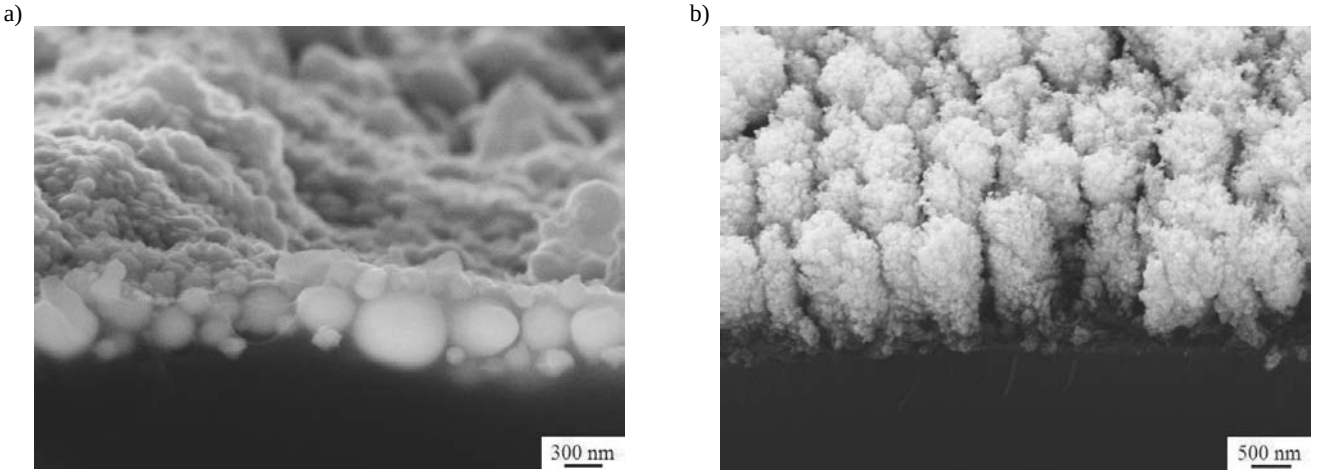

Fig. 25. SEM fracture images of the front contact layer from: a) the A paste onto an Si substrate without texture and an ARC layer by selective laser sintering with the laser beam of 40.5 W and the laser beam feed rate of 50 mm/s, b) B paste on an Si substrate without texture and with an ARC layer by selective laser sintering with the laser beam of 24.3 W and the laser beam feed rate of 50 mm/s

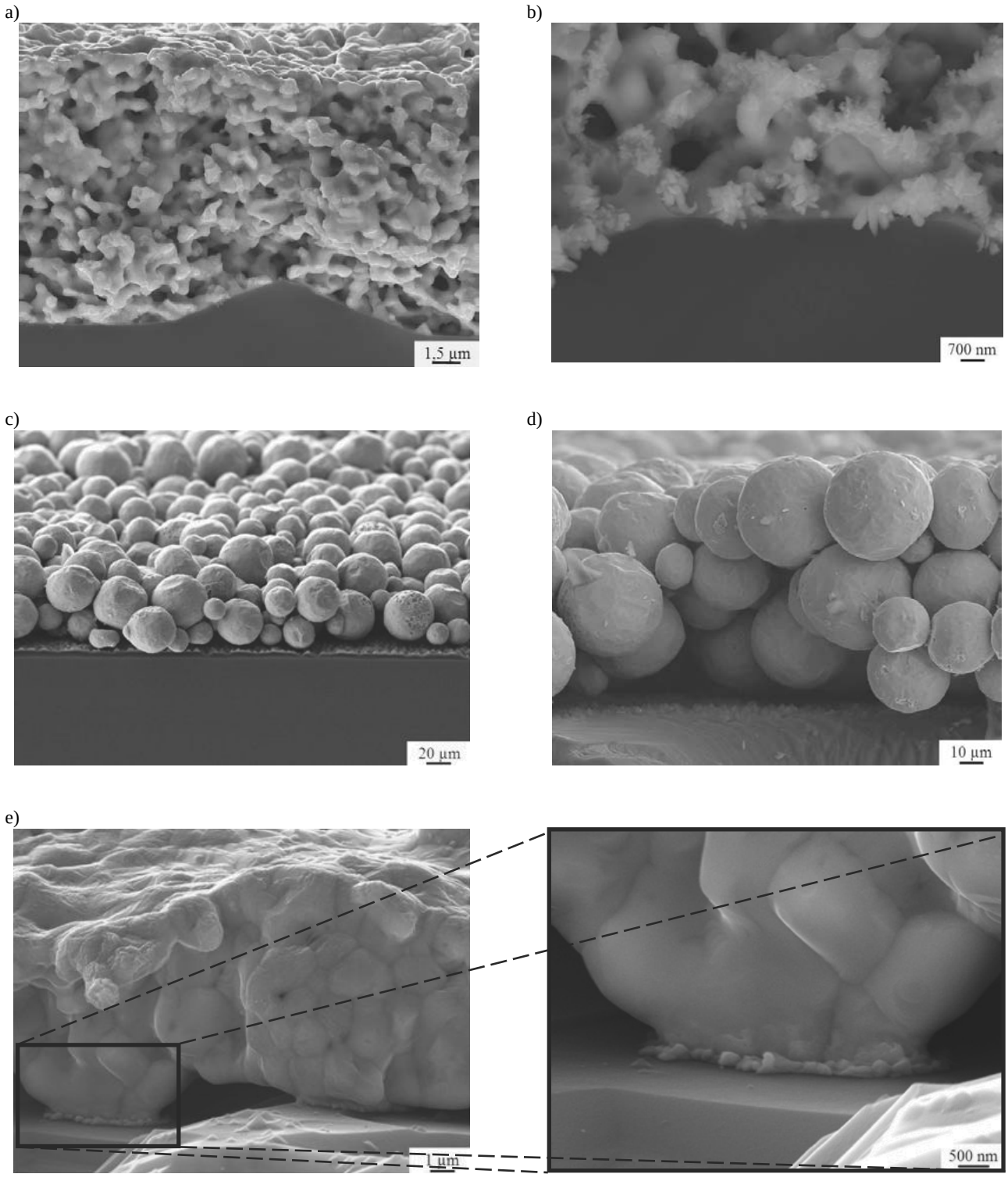

Fig. 26. SEM fracture images of a front contact layer co-fired in the furnace at the temperature of: a) 830°C, b) 945°C from PV 145 paste on an Si substrate without texture and an ARC layer, c) 830°C, d) 945°C from F paste on an Si substrate with texture and an ARC layer, e) 945°C from C paste on an Si substrate without texture and an ARC layer

The qualitative analysis of phase composition (Fig. 27 b) carried out with the X-ray diffraction method confirms that for electrodes from sintered pastes, layers contain the Ag phase produced as expected. The presence of reflections from an Si phase present in the substrate materials was revealed on X-ray diffractograms established with the Bragg-Brentano technique (Fig. 27 a). We determined with the results of laser micro-treatment investigations that the minimum specific contact resistance of the I, II test electrode system is between 0.17 and 0.53 $\Omega \cdot cm^2$ for those made from silver nanopaste with the average thickness of the deposited electrode layer of 35 μm (Fig. 28).

The lowest specific contact resistance value for the studied front contacts prepared from different pastes was seen for the selective laser sintering method of between 0.17 and 0.53 $\Omega \cdot cm^2$ for the following I, II test electrode systems as compared to co-firing in the furnace where resistance was 1.08 and 0.48 $\Omega \cdot cm^2$ for the I, II test electrode systems (Fig. 29).

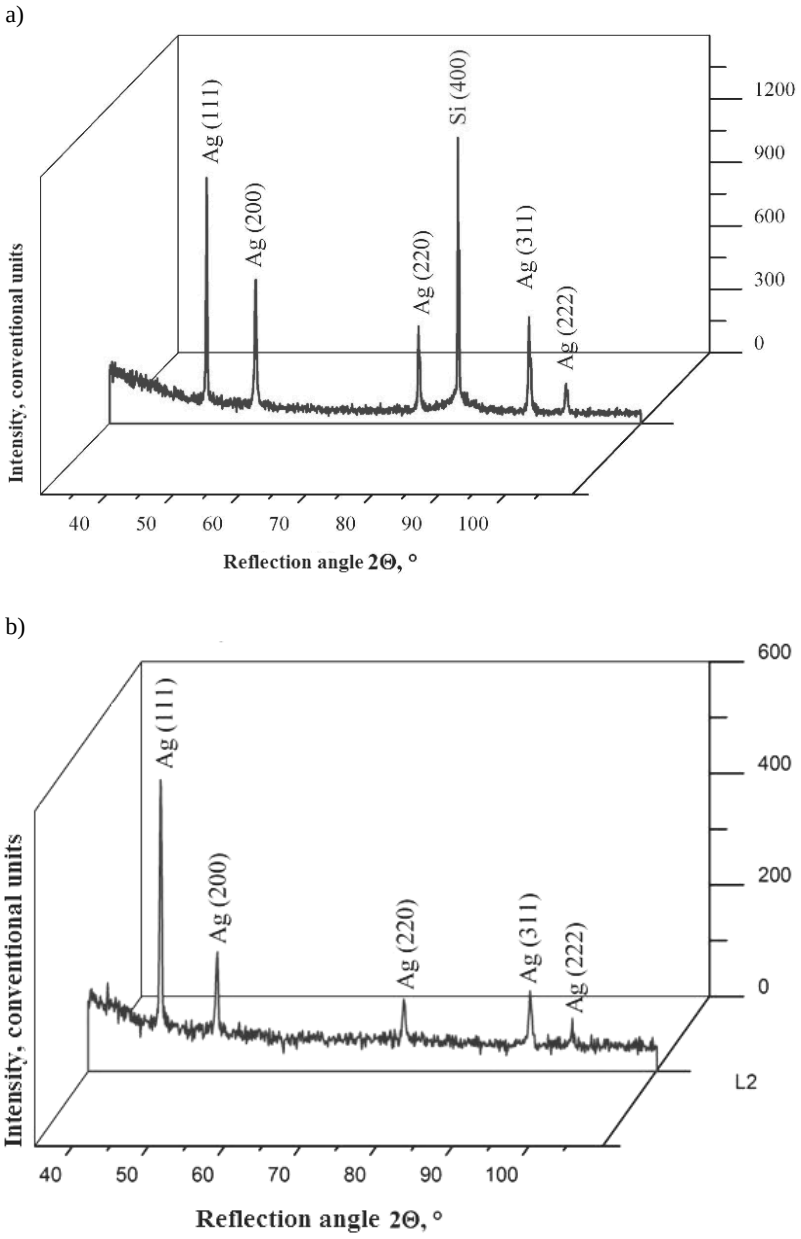

Fig. 27. X-ray diffraction pattern of front metallisation made from silver paste based on silver powder onto a surface without texture and with ARC layer selective laser sintering with the laser beam of 40.5 W and the laser beam feed rate of 50 mm/s with: a) Bragg – Brentano technique, b) SKP technique (α=8°)

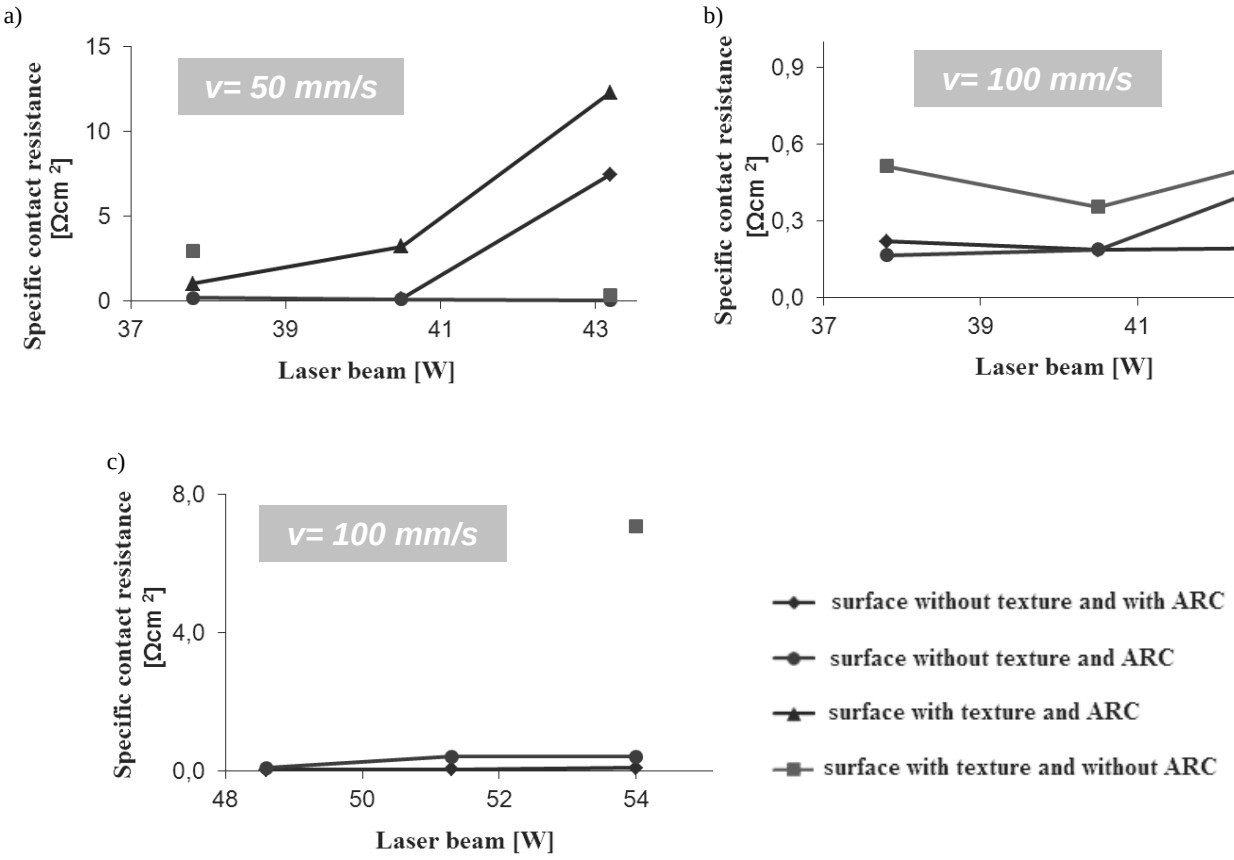

Fig. 28. Specific contact resistance depending on laser micro-treatment conditions with electrodes made from the paste based on a) silver, b) nanopowder, c) powder

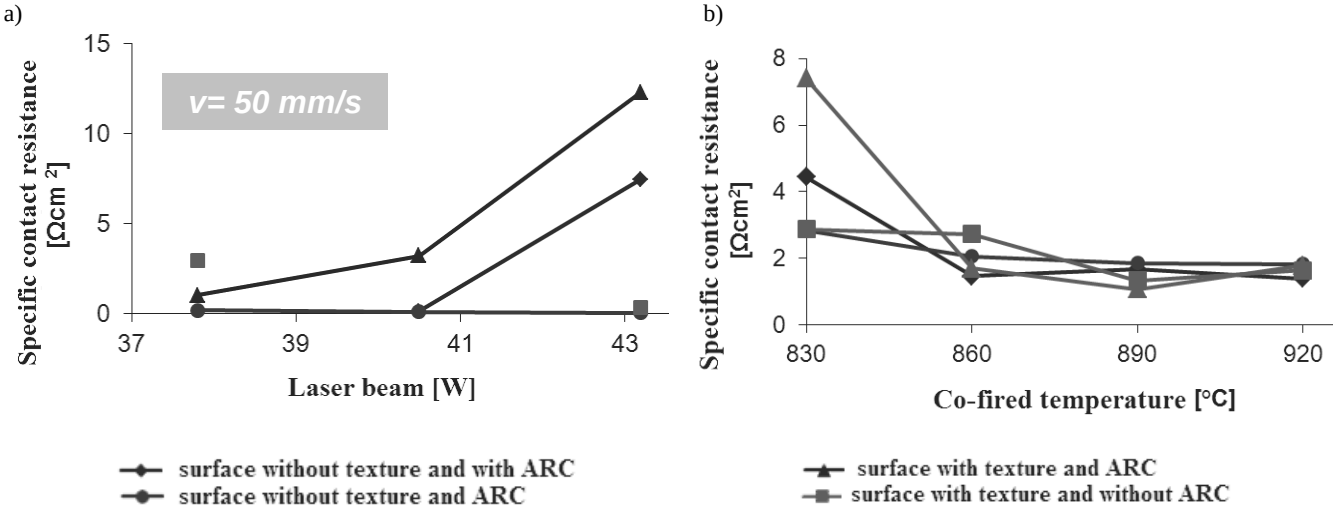

Fig. 29. Comparison of the smallest values of specific contact resistance depending on the applied manufacturing method of the front contacts: a) electrodes subjected to selective laser sintering made from silver nanopaste, co-fired in the furnace electrodes made from the PV 145 paste

We can determine the uncertainty range of the measured resistance based on the parameters of a multimeter and calibrator. Table 3.6 gives measurement parameters for the apparatuses.

In our case:

- boundary error $\pm\Delta U$ of voltmeter:

  $\Delta U = \pm(0.02\%\ set\ of\ value + 2\ numbers)$

  Assumed to be an extremely disadvantageous case, where:
  a set of value = range = 5 V
  the value of 2 numbers in the range of: $5\,V = 2 \cdot 0.01\,mV$
  so $\Delta U = \pm(0.02\% \cdot 5\,V + 2 \cdot 0.01\,mV) = \pm 1.2\ mV$

- boundary error $\pm\Delta I$ of calibrator:

  $\Delta I = \pm(0.1\%\ set\ of\ value + 6\ numbers)$

  Assumed to be an extremely disadvantageous case, where:
  set of value = range = 110 mA
  a value of 6 numbers in the range of: $110\ mA = 6 \cdot 0.01\ mA$
  so $\Delta I = \pm(0.1\% \cdot 110\ mA + 6 \cdot 0.01\ mA) = \pm 0.17\ mA$

The study assesses all complex uncertainty measurement results for the measured resistance of the test electrodes prepared from silver pastes and using a convectional and non-conventional method on surfaces with different morphology. Table 3.7 gives an example of a complex uncertainty measurement results estimation connected with the obtained investigation results for the measured resistance of the I test electrodes system deposited from silver paste co-fired in the furnace on a monocrystalline surface.

It was determined in the computational investigations of the u_C standard complex uncertainty of measurement results obtained with technical methods that in case of the A, B, C, D, E, F silver pastes applied and the commercial PV 145 paste, the dominating standard uncertainty was of B-type (i.e., connected with imperfection of the measuring apparatus). Two tables were found also from which it is difficult to determine which u_C standard complex uncertainty component is dominant (u_A or u_B) (Table 3.8).

The paper describes silicon solar cells with front metallisation designed and developed at the Institute of Engineering Materials and Biomaterials prepared from commercial and prepared pastes based on the best results of specific resistance of front contacts measured using the transmission line method on the measurement site.

Table 3.6.
Specifications of apparatuses

Name	Type	Range	Accuracy
Multimeter (numerical)	BM859CF	0-50 V	± (0.02% set of values + 2 numbers)
Calibrator	C401B	0-110 mA	± (0.1% set of values + 6 number)

Table 3.7.
Results of the standard complex uncertainty (for I=10 mA, ΔI=0.17 mA, ΔU=1.2 mV, a complex certainty level α=0.05 value k_α=1.645) of the front electrodes co-fired in the furnace from the standard PV 145 paste on a textured surface and deposited on the ARC layer photovoltaic solar cells (chosen example)

Sample symbol	Distance between electrodes, cm	Arithmetic mean $\overline{R_T}, \Omega$	Standard deviation of arithmetic mean	$u_A(R_T)$	$u_B(R_T)$	$u_C(R_T)$	$\overline{R_T} \pm k_\alpha u_C(R_T)$
A9	0. 25	20.63	0.003	0.01	0.21	0.21	20.63 ± 0.35
A10		9.75	0.006	0.02	0.12	0.12	9.75 ± 0.20
A11		8.51	0.003	0.01	0.11	0.11	8.51 ± 0.18
A12		9.50	0.009	0.04	0.12	0.12	9.50 ± 0.20
A9	0.5	17.55	0	0	0.19	0.19	17.55 ± 0.31
A10		15.19	0.009	0.04	0.16	0.17	15.19 ± 0.28
A11		14.48	0.003	0.01	0.16	0.16	14.48 ± 0.26
A12		15.30	0.009	0.04	0.17	0.17	15.30 ± 0.28
A9	1	26.91	0.015	0.06	0.27	0.28	26.91 ± 0.46
A10		23.43	0.009	0.04	0.24	0.24	23.43 ± 0.40
A11		22.78	0.003	0.01	0.23	0.23	22.78 ± 0.39
A12		23.54	0.003	0.01	0.24	0.24	23.54 ± 0.40
A9	2	42.91	0.018	0.08	0.43	0.43	42.91 ± 0.71
A10		38.35	0.015	0.07	0.38	0.39	38.35 ± 0.64
A11		37.25	0.009	0.04	0.37	0.37	37.25 ± 0.62
A12		37.62	0.018	0.08	0.38	0.38	37.62 ± 0.63

Table 3.8.
Results of the standard complex uncertainty (for I=10 mA, ΔI=0.17 mA, ΔU=1.2 mV, complex certainty level α=0.05 value k_α=1.645) of the front electrodes subjected to selective laser sintering using the laser beam of: 21.6; 24.3; 27 W and the laser beam feed rate of 50 mm/s for the B paste on a surface textured with the coated ARC layer solar cells

Sample symbol	Distance between electrodes, cm	Arithmetic mean $\overline{R_T}$, Ω	Standard deviation of arithmetic mean	$u_A(R_T)$	$u_B(R_T)$	$u_C(R_T)$	$\overline{R_T} \pm k_\alpha u_C(R_T)$
L56	0.8	4.47	0	0.00	0.08	0.08	4.47 ± 0.13
L57		5.42	0	0.00	0.09	0.09	5.42 ± 0.14
L56	0.4	7.20	0	0.00	0.10	0.10	7.20 ± 0.16
L57		7.52	0.667	2.87	0.10	2.87	7.52 ± 5.63
L56	0.2	19.46	0.333	1.43	0.20	1.45	19.46 ± 2.84
L57		16.50	0.333	1.43	0.18	1.45	16.50 ± 2.83
L56	0.1	30.25	0.333	1.43	0.30	1.47	30.25 ± 2.87
L57		29.53	0	0.00	0.30	0.30	29.53 ± 0.49

A quest for the new feasible applications of laser treatment in photovoltaics has proved that the I, II test electrode system subjected to selective laser sintering minimised the resistance in the connection zone of the front electrode with the silicon surface as compared to the I, II test electrode system test electrode system co-fired in the furnace. It is necessary to emphasise that further efforts devoted to this issue will undoubtedly result in the high efficiency of the solar cells manufactured in the industrial practice.

The electrical properties of solar cells with the front electrode made from the PV 145 paste, co-fired in the furnace in the temperature of 770 to 920°C, determined with I-V curves confirmed that their efficiency is E_{ff}=0.05-15.90% (Fig. 30 a, b, Table 3.9). The high efficiency of solar cells (E_{ff}=15.80-15.90%) was determined on a substrate with texture and an ARC layer (Table 3.9). The following reduced short circuit current value was obtained (I_{sc}) of 799 mA and open-circuit voltage (U_{oc}) of 388 mV in solar cells with the lowest efficiency. It was found based on electrical properties that the surface morphology has a significant effect on the conversion rate of solar energy into electrical energy by a solar cell. An average fill factor of the solar cells (0.65 FF) manufactured on silicon without texture is smaller than the factor (0.74 FF) for the solar cells prepared on silicon with texture.

The electrical properties of the solar cells with the front electrode made from the F paste, co-fired in the furnace at 945°C, determined from curves I-V proved that their efficiency was E_{ff}=0.30-0.70% (Fig. 31 a, Table 3.10). The efficiency of the solar cells with the front electrode made from the C paste and co-fired in the furnace at 770 to 945 C is E_{ff}=0.50-2.30% (Fig. 32 a, Table 3.11). A reduced short-circuit current (I_{sc}) value of about 279 mA and open-circuit voltage (U_{oc}) of about 103 mV was obtained for the solar cells with the smallest efficiency. These solar cells demonstrated low efficiency in both cases according to co-firing temperature and surface morphology on which they are printed and a comparable fill factor is approx. 0.3 (FF).

The electrical properties of the solar cells with the front electrode made from PV 145 (Table 3.12), F (Table 3.13) and C (Table 3.14) pastes and co-fired in the conveyor furnace determined from IV curves using a two-diode model have ascertained the A_1 factor value is 1 for all calculations, however, the A_2 factor value is 1.88-5.66 for the solar cells co-fired at 920-945°C. However, the ε factor value is 0.33-3.54%. This confirms the average consistency of experimental curves with theoretical curves. It was found based on the measurements that the series resistance of the photovoltaic cells co-fired in the furnace from the PV 145 paste between 770 to 920°C (Table 3.12) is 0.05-15.90 Ω, however, the value of dark current, i.e. I_{s1} is $7.78 \cdot 10^{-3}$-$5.63 \cdot 10^{-5}$ and I_{s2} is $(21.63\text{-}29.25) \cdot 10^{-3}$. The smaller values of series resistance obtained for the solar cells co-fired in the furnace at 920°C from wafers with texture (R_s =0.02 Ω) (Table 3.12) confirm the better quality of metal – silicon contacts as compared to the solar cells without texture (R_s=0.08 Ω).

The measurements have shown that the series resistance of the photovoltaic solar cells where the front electrode was made from the C paste, co-fired in the furnace at 770-945°C (Table 3.14) is 1.05-2.82 Ω, however, the value of dark current, i.e. I_{s1} is $18.46 \cdot 10^{-3}$-$11.94 \cdot 10^{-5}$ and for I_{s2} it is $16.24 \cdot 10^{-2}$-$9.03 \cdot 10^{-3}$.

The defects arising come from the PV 145, F, C pastes, after the high-temperature processes of contacts metallisation. The smallest series resistance of a solar cell co-fired at the highest temperature is, respectively: 0.02 Ω (PV 145 paste), 0.57 Ω (F paste), 1.05 Ω (C paste).

The highest efficiency of a photovoltaic solar cell (15.90%) was attained using the conventional technology with the commercial PV 145 paste for forming the front electrode for a textured surface with an antireflection coating deposited and series resistance of 0.02 Ω. The lower efficiency of solar cells was obtained for the following pastes: C – 2.30% and series resistance of 1.05 Ω as well as F – 0.70% and series resistance of 0.57 Ω on a textured surface without an antireflection coating deposited. Lower efficiencies for photovoltaic solar cells produced were probably caused by the lack of a binder in silver paste composition binding the particles together and to the substrate.

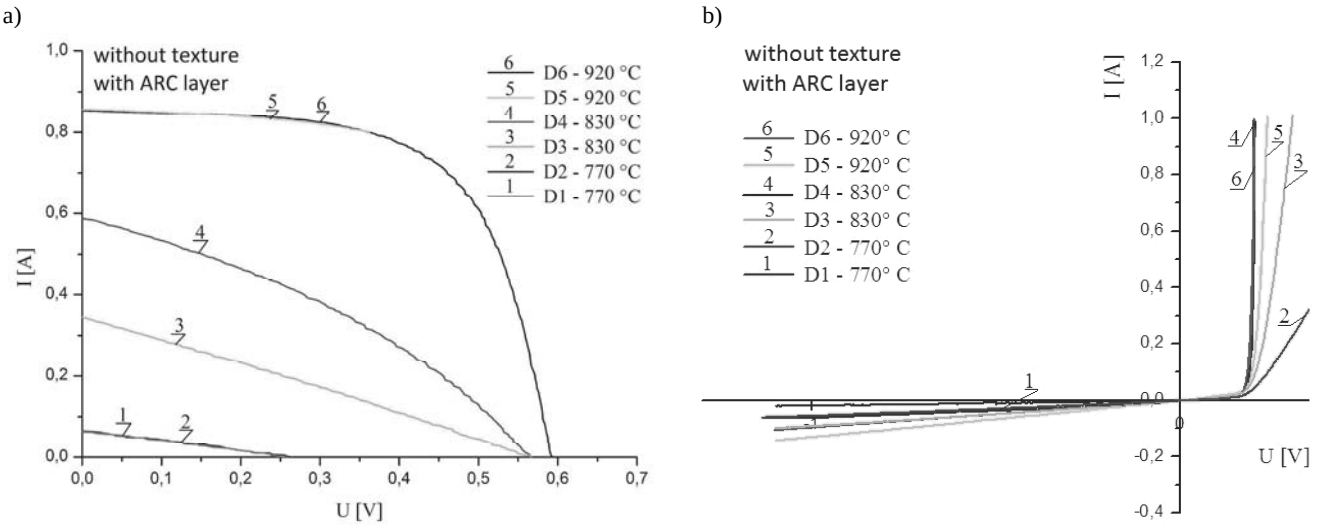

Fig. 30. I-V curves (a − light, b − dark) of solar cells co-fired at different temperature in furnace from PV 145 paste

Table 3.9.
Electrical properties of the silicon solar cells co-fired in furnace from the PV 145 paste

Solar cell symbol	Co-firing temperature, °C	Electrical parameters						
		U_{oc}, mV	I_{sc}, mA	I_m, mA	U_m, mV	P, mW	FF	E_{ff}, %
Photovoltaic solar cell without texture with ARC layer								
D1	770	202.70	67.69	6.41	208.20	1.34	0.101	0.10
D2		202.69	67.73	6.43	208.16	1.34	0.101	0.05
D3	830	564.23	344.53	169.88	305.28	51.86	0.267	2.07
D4		563.86	588.72	354.41	327.22	115.97	0.349	4.64
D5	920	590.93	866.76	740.32	451.76	334.45	0.653	13.38
D6		592.10	856.32	723.44	452.73	327.53	0.646	13.10
Photovoltaic solar cell with texture and an ARC layer								
D7	920	591.5	905.65	819.444	483.1	395.87	0.739	15.80
D8		591.8	902.27	824.195	483.6	398.57	0.746	15.90

I_{sc} – short circuit current of solar cell, I_m – current in maximum power point of solar cell, U_m – voltage in maximum power point of solar cell, U_{oc} – open-circuit voltage of solar cell, FF – fill factor of solar cell, P – power of solar cell, E_{ff} – efficiency of solar cell

Table 3.10.
Electrical properties of silicon solar cells co-fired in the furnace from F paste

Solar cell symbol	Co-firing temperature, °C	Electrical parameters						
		U_{oc}, mV	I_{sc}, mA	I_m, mA	U_m, mV	P, mW	FF	E_{ff}, %
Photovoltaic solar cell with texture and without ARC layer								
E1	945	365.70	68.60	33.68	193.40	6.51	0.26	0.30
E2		568.20	102.75	55.05	326.80	17.99	0.31	0.70

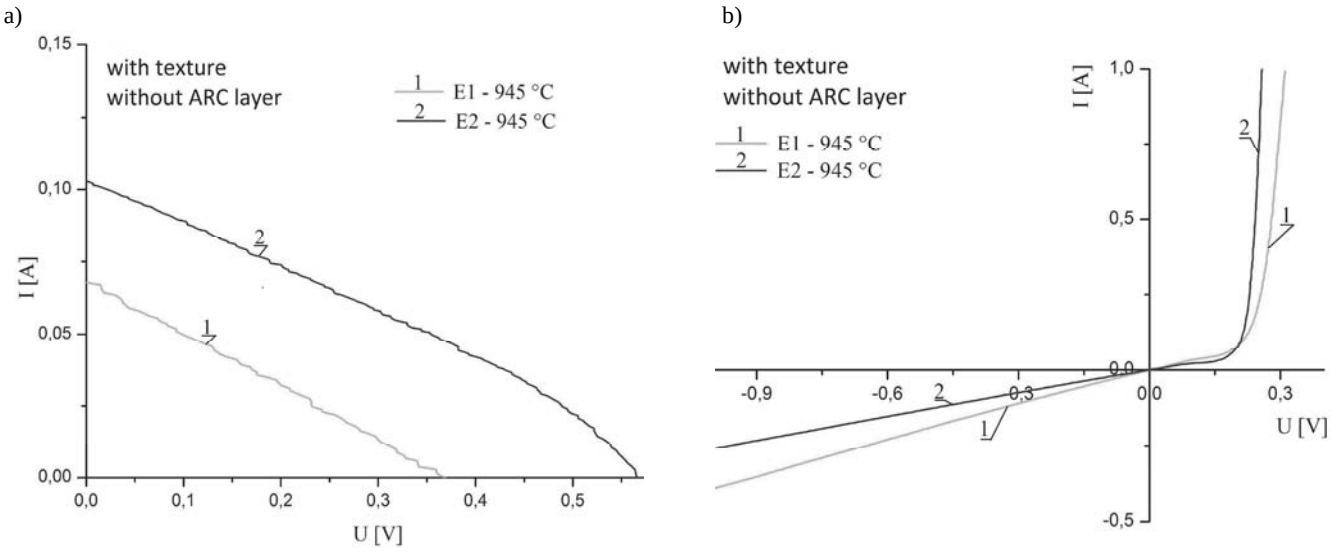

Fig. 31. I-V curves (a − light, b − dark) of solar cells co-fired at different temperature in furnace from F paste

Table 3.11.
Electrical properties of the silicon solar cells co-fired in the furnace from the C paste

Solar cell symbol	Co-firing temperature, °C	Electrical parameters						
		U_{oc}, mV	I_{sc}, mA	I_m, mA	U_m, mV	P, mW	FF	E_{ff}, %
Photovoltaic solar cell without texture and with ARC layer								
F1	770	465.60	113.59	57.35	238	13.65	0.26	0.50
F2		556.60	163.61	88.34	268.70	23.74	0.26	0.90
F3	800	478	197.51	101.60	253.60	25.74	0.27	1
F4		477.90	197.72	108.95	237.18	25.84	0.27	1
F5	830	556.80	208.88	103.49	285	29.50	0.25	1.20
F6		548.80	182.71	91.76	314.50	28.86	0.29	1.20
F7	860	552.40	205.13	104.34	307.90	32.13	0.28	1.30
F8		557.70	216.39	87.62	376.20	32.97	0.27	1.30
F9	890	567.20	325.75	161.86	287.90	46.60	0.25	1.90
F10		534.20	317.50	164.41	264.70	43.51	0.26	1.70
F11	920	577	312.94	134.12	345.30	46,.31	0.26	1.90
F12		570.50	302.48	150.08	322.60	48.41	0.28	1.90
F13	945	569.40	392.80	201.63	295	59.48	0.27	2.40
F14		570	373.27	198.35	285.30	56.58	0.27	2.30

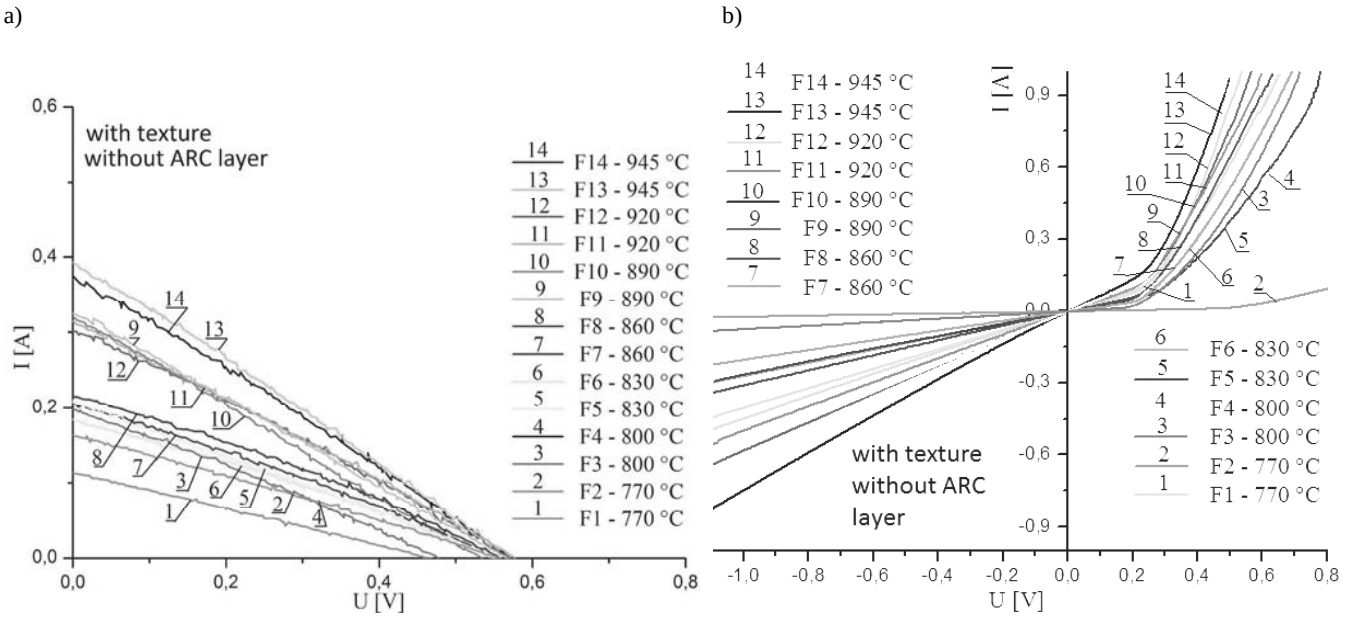

Fig. 32. I-V curves (a − light, b − dark) of solar cells co-fired at different temperature in furnace from C paste

Table 3.12.
Electrical parameters of the photovoltaic solar cells co-fired in the furnace from the PV 145 paste based on I-V curve for the chosen solar cells to the theoretical two-diode model

Solar cell symbol	Co-firing temperature, °C	Electrical parameters							
		I_p, mA	R_{sh}, Ω	R_s, Ω	I_{s1}, A	I_{s2}, A	A_1	A_2	ε, %
Photovoltaic solar cell without texture with ARC layer									
D1	770	103.01	8.64	2.97	3.45e-7	1.47e-4	1	1.80	43.60
D2		71.08	88.64	3.55	3.14e-6	3.21e-5	1	1.33	87.81
D3	830	721.45	1.29	0.29	4.88e-11	4.60e-6	1	2.03	3.79
D4		939.58	0.83	1.37	6.55e-11	3.05e-6	1	2.07	2.02
D5	920	859.54	12.02	0.08	3.32e-11	4.90e-5	1	2.50	0.38
D6		859.28	11.68	0.05	3.37e-11	4.34e-5	1	2.48	0.33
Photovoltaic solar cell with texture and an ARC layer									
D7	920	905.52	109.00	0.02	7.21e-11	7.32e-5	1	2.88	0.21
D8		906.58	95.13	0.02	5.96e-11	8.50e-6	1	2.19	0.19

R_{sh} – parallel resistance of solar cell, R_s – series resistance of solar cell, I_{s1} – saturation current (diode D_1) ingredient of the diffusion dark current, I_{s2} – saturation current (diode D_2) ingredient of the generative recombinant dark current, $A_{1,2}$ – diode quality factors, ε – fitting factor, ε – determines an accuracy of matching the experimental IV curve to the theoretical curve in a two-diode model of a photovoltaic solar cell. It is the difference in the surface between the experimental and theoretical curves with relation to the surface described by the experimental curve between I and V axes [19]

Table 3.13.
Electrical parameters of the photovoltaic solar cells co-fired in the furnace from the F paste assigned based on matching the I-V curve of the chosen solar cells to the theoretical two-diode model

Solar cell symbol	Co-firing temperature, °C	Electrical parameters							
		I_p, mA	R_{sh}, Ω	R_s, Ω	I_{s1}, A	I_{s2}, A	A_1	A_2	ε, %
Photovoltaic solar cell with texture and without ARC layer									
E1	945	246.81	1.52	4.17	3.06e-8	1.99e-3	1	5.52	0.81
E2		110.84	7.63	0.57	3.22e-12	6.97e-7	1	2.04	2.31

Table 3.14.
Electrical parameters of photovoltaic solar cells co-fired in the furnace from C paste assigned based on fitting I-V curve of chosen solar cells to the theoretical two diode model

Solar cell symbol	Co-firing temperature, °C	Electrical parameters							
		I_p, mA	R_{sh}, Ω	R_s, Ω	I_{s1}, A	I_{s2}, A	A_1	A_2	ε, %
Photovoltaic solar cell without texture and with ARC layer									
F1	770	204.79	2.74	1.89	1.13e-9	7.36e-6	1	2.18	6.27
F2		409.69	2.28	2.81	2.63e-10	9.90e-7	1	1.77	2.97
F3	800	487.03	2.18	2.22	2.33e-9	2.52e-6	1	1.69	2.34
F4		407.05	2.19	2.23	2.34e-9	2.52e-6	1	1.68	2.34
F5	830	644.68	1.21	2.23	4.08e-11	2.38e-7	1	1.49	2.00
F6		328.45	2.55	1.92	7.74e-11	1.57e-6	1	1.95	1.63
F7	860	394.75	2.37	1.92	9.73e-11	1.29e-6	1	1.72	2.66
F8		365.35	2.82	1.70	3.21e-10	1.15e-6	1	1.91	3.39
F9	890	746.17	2.32	1.60	1.18e-10	1.80e-5	1	2.22	1.45
F10		588.82	2.05	1.99	1.98e-10	4.95e-6	1	2.05	12.37
F11	920	651.02	2.96	1.63	9.03e-11	3.31e-6	1	1.84	3.00
F12		582.03	2.08	1.51	2.09e-11	4.00e-6	1	1.91	1.88
F13	945	727.74	3.16	1.05	1.64e-11	1.20e-2	1	5.65	1.09
F14		769.74	1.96	1.33	3.59e-10	3.24e-6	1	1.88	3.54

4. Conclusions

The paper has asserted that the laser micro-treatment of the silicon elements of solar cells made from monocrystalline silicon, including the selective laser sintering of front electrode to its surface using the CO_2 laser improves the quality by minimising the connection resistance of the front electrode with the surface.

Laser micro-treatment using CO_2 enables to produce front electrode silicon solar cells with a uniformly melted structure well adhering to the silicon substrate. The electrical properties of the electrodes depend strongly on the presence of particular

components of pastes from which they are prepared. The conductivity of the silver paste examined depends on the grain size, particle shape and the quantity of powder in its composition. Ceramic glaze (SiO_2) joins the base material particles to each other and to the substrate with the remainder being a mixture of an organic carrier ensuring the viscosity of the paste. The thickness of the paste coating and the surface morphology also influence the minimum resistance values in the connection zone between the electrode and silicon.

The following technology-related recommendations have been proposed as a result of the investigations performed. The recommendations relate to the production of the front electrode of silicon solar cells: selecting the optimum nano-silver paste composition − 83%Ag+2%SiO_2+15% of an organic carrier, selecting the average thickness of the deposited layer (35 μm), laser micro-treatment on two test systems – the laser beam of 37.8 W and the laser beam feed rate of 50 mm/s, the surface of a solar cell without texture and an ARC layer. It was determined that the best electrical and structural properties for the analyzed front electrodes are found for the selective laser sintering test system made from nanopaste, however, from the PV 145 paste with the conventional method. Powder with nanometric granulation rather than micrometric one ensures the better stability of the resistance results obtained and also the better structure morphology of the electrode and the connection zone between the electrode and silicon .

References

[1] M.A. Green, Technology and System Applications: Solar cells. Operating Principles, The University of New South Wales, Kensington, 1986.

[2] M.A. Green, A.W. Blakers, S.R. Wenham, S. Narayanan, M.R. Willison, M. Taouk, T. Szpitalak, Improvements in silicon solar cell efficiency, Proceedings of the 19th IEEE Photovoltaic Specialists Conference, Las Vegas, 1985, 39-42.

[3] M.A. Green, A.W. Blakers, S. Narayanan, M. Taouk, Improvements in silicon solar cell efficiency, Solar Cells 17 (1986) 75-83.

[4] M.A. Green, J. Zhao, A. Wang, S.R. Wenham, Progress and outlook for high-efficiency crystalline silicon solar cells, Solar Energy Materials and Solar Cells 65 (2001) 9-16.

[5] M.A. Green, Third generation photovoltaic: solar cells for 2020 and beyond, Physic E 14 (2002) 65-70.

[6] G.A. Landis, Optimization of Tapered Busses for Solar Cell Contacts, Solar Energy 22 (1979) 401-402.

[7] R.S. Scharlack, The Optimal Design of Solar Cell Grid Lines, Solar Energy 23 (1979) 199-201.

[8] H.B. Serreze, Optimizing Solar Cell Performance by Simultaneous Consideration of Grid Pattern Design and Interconnect Configurations, Proceedings of the 13th IEEE Photovoltaic Specialists Conference, PVSEC, Washington, D.C., 1978, 609-614.

[9] R. Hezel, High-efficiency OECO Czochralski-silicon solar cells for mass production, Solar Energy Materials and Solar Cells 74 (2002) 25-33.

[10] S.O. Kasap, Optoelectronics and photonics: principles and practices, Prentice Hall, Upper Saddle River, Englewood Cliffs, NJ, 2001.

[11] E.J. Lee, D.S. Kim, S.H. Lee, Ni/Cu metallization for low-cost high efficiency PERC cells, Solar Energy Materials and Solar Cells 74 (2002) 65-70.

[12] N. Mason, O. Schultz, R. Russell, S. Glunz, W. Warta, 20.1% efficient large area cell on 140 micron thin silicon wafer, Proceedings of the 21st European Photovoltaic Solar Energy Conference, EU PVSEC'06, Dresden, Germany, 2006.

[13] N.B. Mason, T.M. Bruton, S. Glledhill, K.C. Heasman, O. Hartley, C. Morilla, S. Roberts, The selection and performance of monocrystalline silicon substrates for commercially viable 20% efficient lid-free solar cells, Proceedings of the 29th European Photovoltaic Solar Energy Conference, EU PVSEC'04, Paris, France, 2004.

[14] N.B. Mason, D. Jordan, High efficiency silicon solar cell production technology, Proceedings of the 10th European Photovoltaic Solar Energy Conference, EU PVSEC'91, Lisbon, Portugal, 1991, 280-283.

[15] J. Adamczewska, Technological processes in semiconductor engineering, WNT, Warsaw, 1980 (in Polish).

[16] Z.M. Jarzębski, Solar energy, Photoelectrical conversion, PWN , Warsaw, 1990 (in Polish).

[17] F. Kowtoniuk, J.A. Koncewoj, Measurement of semi-conductor material parameters, PWN, Warsaw, 1973 (in Polish).

[18] P. Panek, M. Lipiński, E. Bełtowska-Lehman, K. Drabczyk, R. Ciach, Industrial technology of monocrystalline silicon solar cells, Opto-Electronics Review 11 (2003) 269-275.

[19] P. Panek, Modeling the structure of porous silicon in aspect electrical and optical properties solar cell, PhD dissertation, Institute Library of Metallurgy and Material Science of Polish Academy of Sciences, 2006 (in Polish).

[20] B. Lim, S. Hermann, K. Bothe, J. Schmidt, R. Brendel, Solar cells on low-resistivity boron-doped Czochralski-grown silicon with stabilised efficiencies of 20%, Applied Physics Letters 93/16 (2008) 960-968.

[21] S.S. Cohen, Contact resistance and methods for its determination, Thin Solid Films 104 (1983) 361-379.

[22] M.W. Denhoff, N. Droleta, The effect of the front contact sheet resistance on solar cell performance, Solar Energy Materials and Solar Cells 93/9 (2009) 1499-1506.

[23] K. Rajkanan, J. Shewchun, A better approach to the evolution of the series resistance of solar cells, Solid State Electronics 22 (1979) 193-197.

[24] D.K. Schroder, D.L. Meier, Solar cell contact resistance − a review, IEEE Transactions on Electron Devices 31/5 (1984) 637-646.

[25] A.D. Dobrzańska-Danikiewicz, A. Drygała, Strategic development perspectives of laser processing on polycrystalline silicon surface, Archives of Materials Science and Engineering 50/1 (2011) 5-20.

[26] P. Zięba, P. Panek, K. Drabczyk, M. Lipiński, Training materials. Dissemination achievements of polish and world photovoltaic in education process on higher level, Photovoltaic Laboratory of Institute of Metallurgy and

Material Science, Polish Academy of Sciences, Cracow, 2009.
[27] W. Kuźmicz, Systems and electronic systems, WNT, Warsaw, 1985 (in Polish).
[28] A. Swit, J. Pułtorak, Semiconductor devices, WNT, Warsaw, 1979 (in Polish).
[29] P.P. Altermatt, A.G. Aberle, J. Zhao, A. Wang, G. Heiser, A numerical model of p-n junctions bordering on surfaces, Solar Energy and Solar Cells 74 (2002) 165-174.
[30] H.J. Booth, Recent application of pulsed lasers in advanced material processing, Thin Solid Films 453-454 (2004) 450-457.
[31] T.M. Bruton, Current status: production of efficiency monocrystalline silicon solar cells, Renewable Energy 6/3 (1995) 299-302.
[32] M. Castro, I. Antón, G. Sala, Pilot production of concentrator silicon solar cells: Approaching industrialization, Solar Energy Materials and Solar Cells 92 (2008) 1697-1705.
[33] F. Delahaye, M. Löhrmann, M. Bauer, Edge isolation: Innovative inline wet processing ready for industrial production, Proceedings of the 19th IEEE Photovoltaic Solar Energy Conference, PVSC'04, Paris, France, 2004, 416-418.
[34] M.W. Denhoff, N. Droleta, The effect of the front contact sheet resistance on solar cell performance, Solar Energy Materials and Solar Cells 93/9 (2009) 1499-1506.
[35] L.A. Dobrzański, A. Drygała, K. Gołombek, P. Panek, E. Bielańska, P. Zięba, Laser surface treatment of multi-crystalline silicon for enhancing optical properties, Journal of Materials Processing Technology 201 (2008) 291-296.
[36] L.A. Dobrzański, A. Drygała, Materials for solar cells – state of the art and perspectives, Proceedings of the 12th International Scientific Conference "Achievements in Mechanical and Materials Engineering" AMME'2003, Gliwice – Zakopane, 2003, 311-316.
[37] L.A. Dobrzański, A. Drygała, P. Panek, M. Lipiński, P. Zięba, Development of the laser method of multi-crystalline silicon surface texturization, Archives of Materials Science and Engineering 38/1 (2009) 5-11.
[38] F. Duericks, J. Szlufcik, Defect passivation of industrial multicrystalline solar cells based on PECVD silicon nitride, Solar Energy Materials and Solar Cells 72/1-4 (2002) 231-246.
[39] R. Ebert, P. Regnefuss, L. Hartwig, S. Klötzer, H. Exner, Process Assembly for µm-scale SLS, Reaction Sintering, and CVD, Proceedings of the 4th International Symposium "Laser Precision Micro-fabrication", Munich, 2003, 183-188.
[40] T. Rodacki, A. Kandyba, Processing of energy in solar power station, WPŚ, Gliwice, 2000 (in Polish).
[41] E. Klugmann-Radziemska, Photovoltaic in theory and practice, BTC, Legionowo, 2010 (in Polish).
[42] M. Alemán, A. Streek, P. Regenfuβ, A. Mette, R. Ebert, H. Exner, S.W. Glunz, G. Willeke, Laser micro-sintering as a new metallization technique for silicon solar cells, Proceedings of the 21st European Photovoltaic Solar Energy Conference, EU PVSEC'06, Dresden, Germany, 2006, 705.
[43] F. Dross, K.E. Van, C. Allebe, A. Van der Heide, J. Szlufcik, G. Agostinelli, P. Choulat, H.F.W. Dekkers, G. Beaucarne, Impact of Rear-Surface Passivation on MWT Performances, Proceedings of the 4th IEEE Photovoltaic Energy Conversion World Conference, 2006, 1291-1294.
[44] L. Gautero, M. Hofmann, J. Rentsch, A. Lemke, S. Mack, J. Seiffe, J. Nekarda, D. Biro, A. Wolf, B. Bitnar, J.M. Sallese, R. Preu, All-screen-printed 120-µm-thin large-area silicon solar cells applying dielectric rear passivation and laser-fired contacts reaching 18% efficiency, Proceedings of the 34th IEEE Photovoltaic Specialists Conference, PVSC, 2009, 1888-1893.
[45] S.B. Ghozati, A.U. Ebong, C.B. Honsberg, S.R. Wenham, Improved fill-factor for the double-sided buried-contact bifacial silicon solar cells, Solar Energy Materials and Solar Cells 51 (1998) 121-128.
[46] S.W. Glunz, J. Dicker, M. Esterle, M. Hermle, J. Isenberg, F. Kamerewerd, J. Knobloch, G. Willeke, High-efficiency silicon solar cells for low-illumination applications, Proceedings of the 29th IEEE Photovoltaic Specialists Conference, PVSC, New Orleans, 2002, 450-453.
[47] S.W. Glunz, J. Knobloch, C. Hebling, W. Wettling, The range of high-efficiency silicon solar cells fabricated at Fraunhofer Institut für Solare Energisysteme, Proceedings of the 25th IEEE Photovoltaic Specialists Conference, PVSC, 1997, 231.
[48] S.W. Glunz, J. Necarda, H. Mäckel, A. Cuevas, Analyzing back contacts of silicon solar cells by suns-voc-measurements at high illumination densities, Proceedings of the 22nd European Photovoltaic Solar Energy Conference and Exhibition, Milan, 2007.
[49] S.W. Glunz, High-efficiency Crystalline Silicon Solar cells, Advances in Opto-Electrinics (2007) 1-15.
[50] P. Engelhart, N.P. Harder, T. Horstmann, R. Grischke, M. Rüdiger, R. Brendel, Laser ablation of passivating SiN_X layers for locally contacting emitters of high-efficiency solar cells, Proceedings of the 4th IEEE Photovoltaic Energy Conversion World Conference, 2006, 1024-1027.
[51] N.P. Harder, S. Hermann, A. Merkle, T. Neubert, T. Brendemühl, P. Engelhart, R. Meyer, R. Brendel, Laser-processed high-efficiency silicon RISE-EWT solar cells and characterization, Physica Status Solidi C 6/3 (2009) 736-743.
[52] S. Hermann, P. Engelhart, A. Merkle, T. Nuebert, T. Brendemühl, R. Meyer, N.P. Harder, R. Brendel, 21.4% - Efficient Emitter Wrap-Through RISE Solar Cells on a large area and picosecond laser processing of local contact openings, Proceedings of the 22nd European Photovoltaic Solar Energy Conference, Milan, Italy, 2007, 970-973.
[53] H. Haverkamp, H. Knauss, E. Rueland, P. Fath, W. Joose, M. Klenk, C. Marckmann, L. Weber, H. Nussbaumer, H. Burkhardt, Advancements in the development of back contact cell manufacturing process, Proceeding of the 19th European Photovoltaic Solar Energy Conference, EU PVSEC'04, Paris, France, 2004, 967-969.
[54] V.K. Kofron, Photovoltaic cell with junction-free essentially-linear connections to its contacts, Patent USA, No 4 153 907, 1979.
[55] D.H. Neuhaus, A. Münzer, Industrial silicon wafer solar cells, Advances in Opto-Electronics (2007) 1-15.

[56] A.R. Neuhaus, J.H. Bultman, A.C. Tip, W.C. Sinke, Metallization patterns for interconnection through holes, Solar Energy and Solar Cells 65 (2001) 347-353.
[57] L.A. Dobrzański, M. Musztyfaga, A. Drygała, P. Panek, K. Drabczyk, P. Zięba, Manufacturing photovoltaic solar cells using the screen printing method, Proceedings of the 1st National PV Conference, Krynica–Zdrój, 2009, 1-9 (CD-ROM).
[58] L.A. Dobrzański, M. Musztyfaga, A. Drygała, P. Panek, Investigation of the screen printed contacts of silicon solar cells from Transmissions Line Model, Journal of Achievements in Materials and Manufacturing Engineering 41 (2010) 57-65.
[59] L.A. Dobrzański, M. Musztyfaga, A. Drygała, Selective laser sintering method of manufacturing front electrode of silicon solar cell, Journal of Achievements in Materials and Manufacturing Engineering 42 (2010) 111-119.
[60] L.A. Dobrzański, M. Musztyfaga, A. Drygała, A comparative study of both selective laser sintered and screen printed front contacts on monocrystalline silicon solar cells, Proceedings of the 8th Ukrainian-Polish Conference for Young Researches "Mechanics and Informatics", Ukraine, 2011, 168-170.
[61] L.A. Dobrzański, M. Musztyfaga, A. Drygała, Comparison of conventional and unconventional methods for the front side metallization of silicon solar cells, Proceedings of the 14th International Conference "Advances in Materials and Processing Technologies" AMPT 2011, 284.
[62] L.A. Dobrzański, Engineering materials and materials design. Fundamentals of materials science and physical metallurgy, WNT, Warsaw-Gliwice, 2006 (in Polish).
[63] J.P. Boyeaux, H. El. Omari, D. Sarti, A. Laugier, Towards an improvement of screen printed contacts in multicrystaline silicon solar cells, Proceedings of the 11th European Photovoltaic Solar Energy Conference and Exhibition, 1992, 1-4.
[64] M. Burgelman, Thin film solar cells by screen printing technology, Proceedings of the Workshop Micro-technology and Thermal Problems in Electronics, 1998, 129-135.
[65] F. Clement, M. Menkoe, R. Hoenig, J. Haunschild, D. Biro, R. Preu, D. Lahmer, J. Lossen, H.J. Krokoszinski, Pilot-line processing of screen-printed Cz-Si MWT solar cells exceeding 17% efficiency, Proceedings of the 34th IEEE Photovoltaic Specialists Conference, PVSC, 2009, 223-227.
[66] F. Clement, M. Menkoe, D. Erath, T. Kubera, R. Hoenig, W. Kwapil, W. Wolke, D. Biro, R. Preu, High throughput via-metallization technique for multi-crystalline metal wrap through (MWT) silicon solar cells exceeding 16% efficiency, Solar Energy Materials and Solar Cells 94/1 (2010) 51-56.
[67] F. Clement, M. Menkoe, T. Kubera, C. Harmel, R. Hoenig, W. Wolke, H. Wirth, D. Biro, R. Preu, Industrially feasible multi-crystalline metal wrap through (MWT) silicon solar cells exceeding 16% efficiency, Solar Energy Materials and Solar Cells 93/6-7 (2009) 1051-1055.
[68] K. Faika, M. Wagner, P. Fath, E. Bucher, Simplification of EWT (emitter wrap-through) solar cell fabrication using Al-P-co-diffusion, Proceedings of the 28th IEEE Photovoltaic Specialists Conference, PVSEC, 2000, 260-263.
[69] P. Hahne, E. Hirth, I.E. Reis, K. Schwichtenberg, W. Richtering, F.M. Horn, U. Eggenweiler, Progress in thick-film pad printing technique for solar cells, Solar Energy Materials and Solar Cells 65/1-4 (2001) 399-407.
[70] D.M. Huljic, S. Thhormann, R. Preu, R. Lüdemann, G. Willeke, Pad printing front contacts for c-Si solar cells-a technological and economical evaluation, Proceedings of the 29th IEEE Photovoltaic Specialists Conference, PVSC, New Orleans, Louisiana, USA, 2002, 126-129.
[71] W. Jooss, H. Knauss, F. Huster, P. Fath, E. Bucher, R. Tölle, T.M. Bruton, Back contact buried contact solar cells with metallization wrap around electrode, Proceedings of the 28th IEEE Photovoltaic Specialists Conference, PVSEC, 2000, 176-178.
[72] P. Vitanov, E. Goranova, V. Stavbrov, P. Ivanov, P.K. Singh, Fabrication of buried contact silicon solar cells using porous silicon, Solar Energy Materials and Solar Cells 93 (2009) 297-300.
[73] S.R. Wenham, M.A. Green, Buried contact solar cells, Australian Patent 570309, March 1985.
[74] Z. Yuwen, L. Zhongming, M. Chundong, H. Shaogi, L. Zhiming, Y. Yuan, Ch. Zhiyun, Buried-contact high efficiency silicon solar cell with mechanical, Solar Energy Materials and Solar Cells 48/1-4 (1997) 167-172.
[75] A.U. Ebong, C. Honsberg, S.R. Wenham, M.A. Green, Mechanically grooved, double sided, buried contact silicon solar cells, Renewable Energy 11/3 (1997) 331-340.
[76] A.U. Ebong, D.S. Kim, S.H. Lee, Low cost double-sided buried contact silicon solar cells, Renewable Energy 11/3 (1997) 285-297.
[77] http://www.ios.krakow.pl
[78] M. Castro, I. Antón, G. Sala, Pilot production of concentrator silicon solar cells: Approaching industrialization, Solar Energy Materials and Solar Cells 92 (2008) 1697-1705.
[79] H. Exner, P. Regnefuss, L. Hartwig, S. Klötzer, R. Ebert, Selective laser sintering with a Novel Process, Proceedings of the 4th International Symposium "Laser Precision Micro-fabrication", Munich, 2003, 145-151.
[80] L. Kukiełka, The basis of engineering investigations, PWN, Warsaw, 2002 (in Polish).